Tuijin Jishu/Journal of Propulsion Technology
ISSN: 1001-4055
Vol. 44 No.5 (2023)

Graphene/Bismuth-Codoped Fe_3O_4 Nanocomposites for UV Light-Assisted Photodegradation of Industrial Dyes Produced by the Coprecipitation Method

J.F.Joe Sherin[a], G.Edwin Sheela[a*]

[a]Research Scholar (Register No. 20113232132005), Department of Physics,

Muslim Arts College, Thiruvithancode-629174, Affiliated to Manonmanium Sundaranar University, Abishekapatti, Tirunelveli-627 012, Tamilnadu, India.

[a*]Department of Physics, Muslim Arts College, Thiruvithancode, Kanyakumari District-629174,

Tamilnadu, India.

Abstract

Industrial dye waste is extremely poisonous, nonbiodegradable, and has a severe detrimental effect on the ecosystem. Graphene-doped Fe_3O_4 nanocomposites (G/F-NCs), undoped Fe_3O_4 nanoparticles (F-NPs), bismuth-doped Fe_3O_4 nanoparticles (Bi/F-NPs) and graphene-bismuth codoped Fe_3O_4 nanocomposites (G/Bi/F-NCs) all successfully photodegrade phenothiazine derivative dyes. The face-centered cubic structure of metallic Fe_3O_4 is confirmed by the X-ray powder diffraction patterns of all the produced samples. The rise in crystallite size in the Bi-doped samples shows that the addition of Bi 4f considerably accelerates the formation of crystalline grains in Fe_3O_4, whereas the addition of graphene dopants causes a decrease in particle size and an expansion of the bandgap. The addition of graphene nanoflakes and the development of secondary pores are credited with giving G/Bi/F-NCs ($90.847 m^2/g$) a larger specific surface area. The presence of oxygen anion, graphene, Bi 4f ion and Fe 3p and Fe 2p oxidation states in the Fe_3O_4 lattice is confirmed by the X-ray photoelectron spectra of O 1s, C1s, Bi 4f and Fe 2p.

Keywords: *graphene-bismuth codoped Fe_3O_4 nanocomposites; XRD; XPS; EDAX*

1.Introduction

The two most pressing challenges in the modern world are environmental pollution and the energy crisis. One of the main issues facing the energy storage sector is the production of energy from materials that are inexpensive. As opposed to that, industrial water-based pollution is the significant environmental issues. Most industrial waste in developed nations contains significant amounts of dyes made using xenobiotic compounds. In these hazardous towards humans, animals, and aquatic life (VanHuyNguyen et al., 2020), difficult to biodegrade, and recalcitrant. Thyazine colours are heterocyclic series with occurrences of sulphur and nitrogen. Specifically, thyazine dyes include methylene blue (MB) (medicine colour) that was typically to be present in industrial waste water and has taken into consideration within this situation due to its substantial side effects and detrimental impacts on the environment (Chandra et al., 2010). Therefore, it is crucial to remove industrial dye from water using inexpensive and environmentally acceptable materials. Due to their numerous physicochemical features, magnetite (Fe_3O_4) nanoparticles have attracted a lot of attention in the research community over the past few years. Because of their chemical strength, magnetic properties, strong oxidative stability, and biocompatibility, magnetic iron oxide nanoparticles are the subject of extensive research. Fe_3O_4 nanoparticles have a wide range of

applications, such as MRI contrast agents, metal ion absorbents in water treatment, hyperthermia therapy, drug delivery, cancer treatment, photomagnetic imaging, the construction of supercapacitor devices, photocatalysis, sensors, etc (Chang et al., 2005; Dubus et al., 2006; Liu et al., 2020; Bharath et al., 2022; Kim et al., 2005; Setiadi et al., 2017; Beji et al., 2010; Kim et al., 2010; Gautam et al., 2017).

Fe_3O_4 (magnetite) is one of the most magnetic nanoparticles. An extensively researched ferrimagnetic oxide with a cubic inverse spinel structure is Fe_3O_4. The dominant mineral content of iron sand is Fe_3O_4 (Jalil et al., 2017; Riana et al., 2018). The electron hopping between the Fe^{2+} and Fe^{3+} ions in the octahedral sites gives it its magnetic and electric characteristics. It is common knowledge that adding transition metal ions to Fe_3O_4 can increase its catalytic activity (Mahdavi et al., 2013). Doping Fe_3O_4 with rare earth or transition metal elements can enhance the magnetic properties of the material (Tsai et al., 2004; Chen et al., 2005; Penc et al., 1999; Li et al., 2004). The structural, magnetic, and transport properties of the related magnetite-based materials are frequently altered by the doping of Fe_3O_4 in thin film samples (Takaobushi et al., 2007; Tripathy et al., 2007; He et al., 2013; Moyer et al., 2011; Chou et al., 2005). Magnetic Fe_3O_4 nanoparticles can be made using a variety of techniques, including hydrothermal synthesis, thermal decomposition, micro-emulsion, co-precipitation, sol-gel, thermal treatment, solvothermal, combustion, ceramic method, soft mechanochemical method, sonochemical method, and microwave-assisted synthesis (Lazarevic et al., 2013; Naseri et al., 2011; Yadav et al., 2017; Agusu et al., 2019; Hu et al., 2006; Hu et al., 2007; Hong et al., 2006; Amara et al., 2009; Tang et al., 2004; Laurent et al., 2008; Matijevicet al., 1975; Deng et al., 2005; Xu et al., 2009).

Due to their biocompatibility and high saturation magnetization, Fe_3O_4 nanoparticles have attracted a lot of attention in the past few decades due to their suitability for a variety of biomedical applications (Qiao et al., 2009; Yang et al., 2009; Lu et al., 2007; Laurent et al., 2008). In the remediation of ground water, particularly for the removal of arsenic, using Fe_3O_4 for separation of water contaminants has become established. To create numerous Fe_3O_4 nanoparticles using the co-precipitation approach, stoichiometric mixes of ferrous and ferric hydroxides were used (Deng et al., 2005). Low temperature, quick reaction times, and high reaction yield are the defining characteristics of this procedure (Yang et al., 2011). The higher SA:V suggested by Fe_3O_4 nanoparticles leads to superior paramagnetic activities, which in turn improves the way of breakdown by lowering the nanoparticles' surface energy and strong dipolar attraction (Liu et al., 2019). Fe_3O_4 is therefore recognised as a crucial factor substances to enable photocatalysis because of its inexpensive, highly sensitive the surface, high rate of electron transfer, and strong capacity for adsorption against harmful water contaminants. These properties also support the use of an exterior magnet and a suitable magnetic partition for the processing or removal of nanocomposites (Balamurugan et al., 2019; Liu et al., 2019). A transition metal oxide's surface characteristics, bonding efficiency, lattice flaws, and electronic and lattice structure can all have a significant impact on how well the material performs as a photocatalyst (Balamurugan et al., 2019; Liu et al., 2019). Adding cations to iron oxide has recently ever been widely developed to adjust the chemical and physical characteristics of Fe_3O_4 nanoparticles, that is increasing the efficiency of both catalysis and energy storage is the force of the bond between metal and oxygen, bulk defect, lattice structure, etc. (Liu et al., 2019; Bharath et al., 2022). In order to further enhance these catalysts' remarkable high visible light responsivity and effective photocatalytic performances, bismuth-related nanoparticles have been modified with metals and non-metals, carbonaceous materials, and biopolymers (Wang et al., 2011). In several photocatalytic processes, including as antifogging, self-cleaning, disinfection, carbon dioxide reduction, organic pollutant degradation in water, hydrogen generation, air purification, and others, modified bismuth-related nanoparticles have been used effectively.

The diamagnetic element bismuth (Bi), which has an atomic number of 83, is found in nature. It is a pentavalent transition metal, and the oxides and sulfurides it forms make up a sizable portion of its commercial resource. There are 26 defects in it related to advanced applications of bismuth. Low electrical resistivity, a high Hall coefficient, and low thermal conductivity are the main characteristics (Khaghani et al., 2017). Materials behave as semiconductors when a thin layer of bismuth is applied to their surfaces (Jones et al., 1936). Once more, it has been found that bismuth expands by around 3% during solidification and is denser in its liquid phase than in the solid phase. Due to its ability to compensate for the contraction of other alloy components, it can be employed as an alloy component (Jones et al., 1936). With a relatively low melting point (271°C), bismuth is also

comparatively non-toxic. About 63% of bismuth is used to make medications, pigments, and cosmetics. According to Pistofidis et al. (2007), 26% of it is also utilised in the metallurgical sector for casting and galvanising. According to Pistofidis et al. (2007), 4% and 7% of bismuth are utilised in research while the remaining 7% is used in bismuth alloys, solders, and ammunition. Bismuth in its cationic +3 oxidation state and nitrate anions make up the salt known as bismuth(III) nitrate. Pentahydrate is the most widely used solid form. Other bismuth compounds can be made using it (Mary et al., 1994). Commercially, it is offered. Because it is the sole nitrate salt produced by a group 15 element, bismuth is considered to be metallic (Green et al., 1997).

Due to its exceptional properties and wide range of uses as adsorbents, thermal transport media, components for biosensors, the active substance used to make supercapacitor electrodes, and electronic parts, graphene is regarded as the most in-demand substance in the research sector (Balamurugan et al., 2018). Doping the material with graphene can improve its thermal stability, chemical resistance, and theoretical surface area of 2600m^2/g (Balamurugan et al., 2016; Chen et al., 2019; Vijayalakshmi et al., 2021; Vermisoglou et al., 2019; Ng et al., 2017). As a result, many energy conversion, storage, and catalytic reactions will be more effective when metal oxides and graphene are combined (Wu et al., 2010; Ashraf et al., 2021). The sonochemical method, the sol-gel method, the microemultion method, the electrospray method, the flow injection method, the hydrochemical process, and the co-precipitation method are just a few of the preparation techniques that are available for the synthesis of Fe_3O_4 nanoparticles (Liang et al., 2020; Hosseini et al., 2013; Anjana et al., 2018). Due to its inexpensive price, environmental friendliness, good product purity and yield, and reproducibility, co-precipitation processes have become one of the most popular synthesis methods (Athar et al., 2015; Cruz et al., 2018).

A single layer of carbon atoms makes up graphene (G), a brand-new class of nanomaterial made from carbon. Due to its exceptional electric, thermal, and mechanical properties, graphene has drawn significant scientific attention in nanotechnology in recent years (Geim et al., 2007). It can be used for a variety of purposes based on these characteristics, such as molecular probes (Wang et al., 2010; Lin et al., 2011), nanocomposites (Wang et al., 2010; Wang et al., 2012), electrochemical sensors (Tang et al., 2009; Wang et al., 2010; Wang et al., 2012), Electronic components, the active substance used to make supercapacitor electrodes, adsorbents, and thermal transport media (Simeonidis et al., 2007; Zhou et al., 2008). Graphene would be a better candidate as an adsorbent for the extraction of benzenoid form compounds because it has multiple delocalized -electron systems that can create a strong - stacking interaction with benzene rings (Han et al., 2012; Zhang et al., 2013; Zhao et al., 2011). It was initially obtained in a lab setting using the "scotch tape" technique (Novoselov et al., 2004). The exceptional properties of graphene include a large specific surface area, outstanding mechanical rigidity, extraordinary electrical transport, and great biocompatibility, suggesting that graphene is a viable electrode modified material (Yang et al., 2010). However, graphene's hydrophobicity prevents it from functioning well in water. Aftabtalab et al. (2015) and Giraldo et al. (2013) found that rGO has good potential as a porous material for seawater desalination—"a rising star" of water purification—which removes various water pollutants like metallic ions, anions, microplastic, nanoparticles, organic chemicals, and biological substrate. Graphene could be changed by being oxidised into graphene oxide (GO) to enhance its dissolving property (Zhao et al., 2015; Lee et al., 2015). By using reducing agents, graphene oxide is converted to reduced graphene oxide (rGO) (Mussa et al., 2020). Graphene-like in many ways, although it might also have some oxygen-containing groups on the surface. According to Sharma et al. (2017), rGO sheets are regarded as a particular variety of chemically produced graphene.

According to Perreault et al. (2015) and Gurunathan et al. (2013), the surface contact-based bioactivity of graphene-based materials through the production of reactive oxygen species (ROS) makes the materials suitable for cytotoxicity-based research. (Santos et al., 2012; Pelin et al., 2017; Hastak et al., 2018; Yang et al., 2019; Jedrzejczak et al., 2017; Gade et al., 2015) reported the outcomes of graphene and graphene mixed with IONPs in the current environment. In 2017, Jedrzejczak-Silicka et al. looked into how DNA integrity and relative viability were affected by graphene and Fe_3O_4. They noted the material's outstanding biocompatibility and indicated its potential for use in the treatment of hyperthermia. The ability of Fe_3O_4/graphene composites to enhance transfer and adsorption qualities has attracted a lot of attention (Wang et al., 2012; Yao et al., 2012). Since the development of a synergistic effect could be expected to have high potential in lithium ion batteries, microwave-absorbing

materials, biomedicine, and supercapacitors (Zhou et al., 2010; Zhang et al., 2014; Ou etval., 2014; Liu et al., 2014), special attention has been paid to graphene/Fe_3O_4 composite film. Purified rGO/Fe_3O_4 nanoparticle dispersion synthesised via the chemical reduction approach is described in (Liang et al., 2010). Graphene/F-NP hybrid films demonstrated superparamagnetic characteristics for potential use as magnetic switches. In addition to improving conductivity and avoiding Fe_3O_4 loss due to volume changes during discharge and charge processes, the reduced graphene oxide is in effective electrical contact with the Fe_3O_4. The hydrothermal approach was used by (Cunqing et al., 2017) to create the Fe_3O_4/graphene nanosheet composite. According to Peik et al. (2014) and Padhi et al. (2017), Fe_3O_4/rGO nanocomposites can be employed as photocatalytic materials, for reducing ions of heavy metals like Cu^{+2}, Zn^{+2}, and Ni^{+2} (Moradinasab et al., 2016), Cr-^{2}, Pb^{2+}(Al et al., 2016; Cao et al., 2015; Wang et al., 2015; Sun et al., 2014), identification of Cd^{+2} (Yu et al., 2014) (Padhi et al., 2017) Ions, phenol degradation, and antimicrobial, biosensing and absorbent for removing dyes from aqueous solutions (Yu et al., 2014) (Namvari et al., 2014;Yang et al., 2015 ; Yang et al., 2018). It might be incorporated into a sensor that can identify the presence of arsenic in waste water treatment and mineral water (Cui et al., 2012; Chimezie et al., 2017). A photo-Fenton type reaction could occur when graphene and Fe_3O_4 are combined, and this approach of commercial colour degradation could be inexpensive, non-toxic, and safe for the environment.

Because it considerably reduces pollutants and produces harmless end products (CO_2 and H_2O), Utilising the photodegradation process to clean commercial waste water (Gupta et al., 2012). Due to their nontoxicity, great effectiveness, stability, and high activity over continuous use, iron oxides have received a lot of attention for a long time (Chin et al., 2007, Mandal et al., 2015; Yavuz et al., 2006). A huge surface area (2600m^2/g), superior mechanical flexibility, and optical transparency have been reported to greatly improve the photodegradation properties of graphene functionalized nanocomposites (Gupta et al., 2012). For the effective removal of heavy metal ions, herbicides, and natural dyes, graphene is attached to the surface of river sand (Gupta et al., 2012). Waste water treatment has been reported to use graphene-Fe_3O_4 to photodegrade contaminants (Karim et al., 2022). The combination of graphene with Fe_3O_4 offers the ability to breakdown industrial dyes in an economical, non-toxic, and environmentally acceptable manner by utilising photo-Fenton type responses. There aren't any in-depth investigations on the photodegradation of coloured dyes by graphene and Fe_3O_4 doped with bismuth. As a result, it is expected that double doping Fe_3O_4 with both graphene (G) and bismuth (Bi) will produce better results than either single element doping or leaving it undoped. To evaluate the degradation of commercial dye, Bi and G are utilised as dopants on Fe_3O_4.

2. Experimental Methods

2.1 Materials

Ferrous Chloride Tetrahydrate ($FeCl_2.4H_2O$), Hexahydrate of Ferric Chloride ($FeCl_3.6H_2O$), from National Scientific Company in Madurai, together with 30% Ammonia solution (NH_3). Both graphene and Bismuth Nitrate $Bi_2(NO_3)_3.5H_2O$ were bought from Sigma-Aldrich. Himedia Laboratories Pvt. Ltd. was the source of the washable reagents. With deionized water, all of the aqueous solutions were made. This experiment used only analytical-quality components that weren't further purified.

2.2 Nanocomposites Preparation

Synthesis of Fe_3O_4 nanoparticles (F-NPs), graphene-doped Fe_3O_4 (G/F-NCs), bismuth-doped Fe_3O_4 (Bi/F-NPs) and graphene-bismuth codoped Fe_3O_4 (G/Bi/F-NCs) nanocomposites

For the preparation of Fe_3O_4 nanoparticles, 0.07 M $FeCl_2.4H_2O$ and 0.14 M $FeCl_3.6H_2O$ they were dispersed in deionized water with constant stirring in a 1:2 molar ratio (Maity et al., 2007; Arakha et al., 2015; Ramanathan et al., 2021). The above-obtained homogenous solution was mixed continuously for one hour at 80°C before the ammonia solution (30%) was added dropwise. A pH metre was used to determine the solution's pH, which was 7. A black coloured precipitate resulted from the reaction's completion. The resulting precipitate was washed three times using distilled water before being calcined with 300 °C for one hour. Furthermore, the produced sample was given the label F-NPs. Utilising the following equation, the complete process may be discussed:

$FeCl_2 + FeCl_3 + 8NH_3 + 4H_2O \rightarrow Fe_3O_4 + 8NH_4Cl$

Following the same procedure as for F-NPs, 0.05 g of graphene was added to the primary homogeneous solution to create the graphene doped Fe_3O_4 nanocomposite. Additionally, the prepared sample's label said "G/F-NCs."

Using the same procedure as for F-NPs, 0.07 g of bismuth nitrate $Bi_2(NO_3)_3.5H_2O$ was added to the primary homogeneous solution to create the bismuth doped Fe_3O_4 nanocomposite. And Bi/F-NPs was written on the prepared sample's label.

As with F-NPs are made via synthesis, 0.05 g of graphene along with 0.07 g of bismuth nitrate $Bi_2(NO_3)_3.5H_2O$ were added to the initial homogeneous solution. The ready sample was identified being G/Bi/F-NCs. The resultant product used for additional characterization. Fig. 1 shows the diagram representation in order to create F-NPs, G/F-NCs, Bi/F-NPs, and G/Bi/F-NCs.

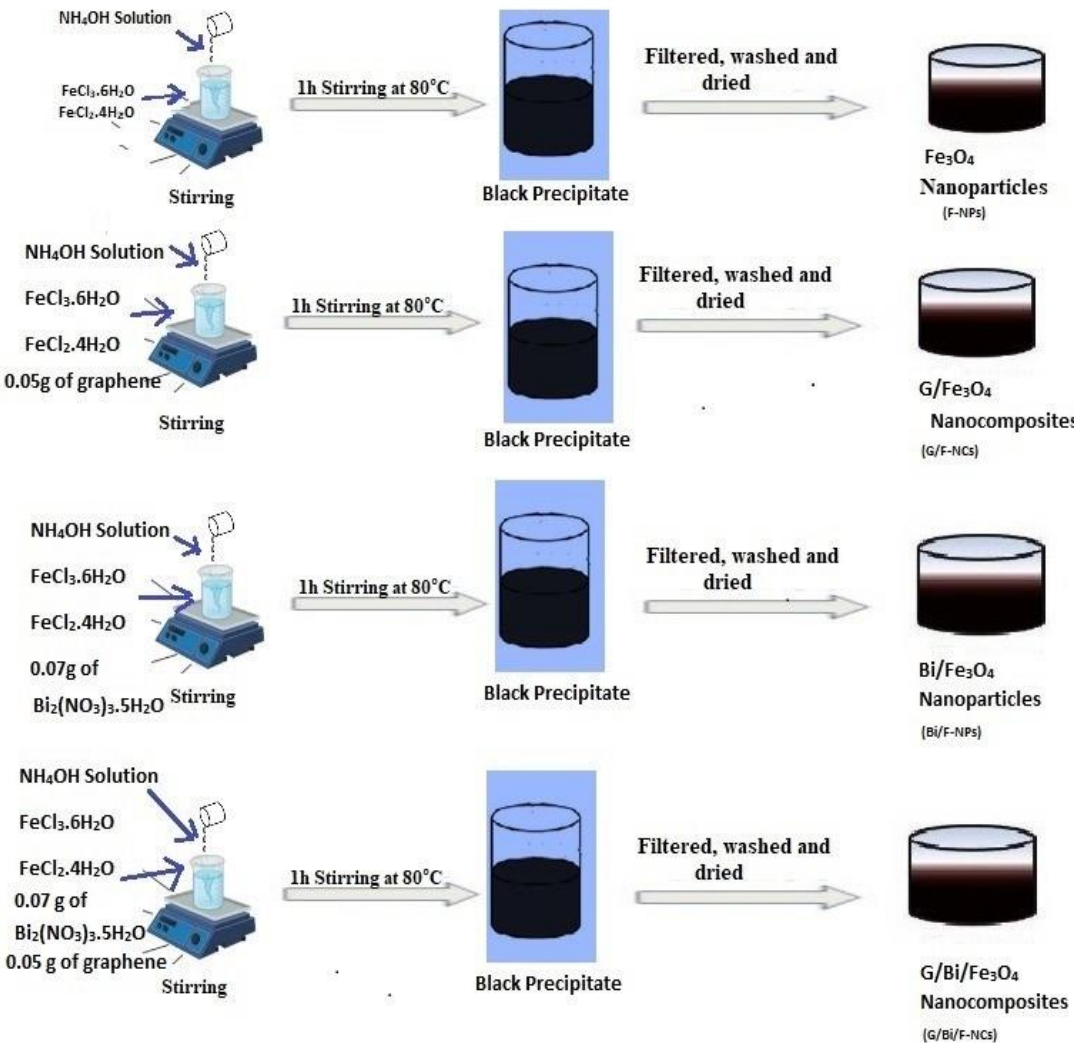

Figure 1 shows a schematic in order to create F-NPs, G/F-NCs, Bi/F-NPs and G/Bi/F-NCs.

2.3 Instrumentation

Utilising a powder X-ray diffraction apparatus (Philips X'pert Pro X-ray diffractometer) equipped using Cu K radiation (= 0.15406 nm), the crystal structure of the produced nanomaterials was studied.

By performing measurements using X-ray photoelectron spectroscopy (XPS) with a Versa Probe II PHI 5000 (bought USA-based ULVAC-PHI Inc.) fitted with a monochromatic Al-K X-Ray source that is microfocused (200 m, 15 KV; hv = 1486.6 eV), the oxidation states within the materials were examined. Using spectroscopy of the UV-visible and photoluminescence (PL), the produced nanoparticles' optical characteristics are examined. Vibrational experiments were conducted using Fourier Transform Infrared Spectroscopy (FT-IR) (Shimadzu FT-IR spectrophotometer). The surface and elemental mapping pictures within the material were captured using EOL JSM-5600 LV scanning electron microscopy. To determine using an element makeup from the synthesised sample, energy dispersive spectroscopy (EDAX) was employed. In order to assess the content's microstructure and particle size, transition electron microscopy and a selected area electron diffraction pattern (SAED) (FEI, TECNAI S twin microscope with a 100 KV acceleration voltage) were both used. Altamira Instruments, Inc.'s Brunauer Emmett Teller (BET) (2 nm–500 nm, mesopore and macro porous analyses) Additives: N_2, Ar To examine the material's BET surface area adsorption and desorption isotherms, degassing temperatures of up to 350° C were used.

The antibacterial activity includes F-NPs, G/F-NCs, Bi/F-NPs and G/Bi/F-NCs against Pseudomonas aeruginosa and Staphylococcus aureus were estimated using the disc diffusion method. All samples were inoculated into sterile nutrient broth (Hi Media) (1.5 mL) and incubated for 2 hours in order to bring the culture up to McFarland standards (108 CFC/mL). Using a sterile spreader, the inocula were applied to brand-new nutrient agar plates. The centre was designated for the control disc. Spreading 100 L of revived culture with a spreader over Mueller-Hinton-Agar/Hi Media resulted in three repetitions of each individual organism. One well with a diameter of 4 mm was inserted with all the prepared samples (50 L). The zones of inhibition (ZOI) were assessed in millimetres after 24 hours of incubation at 37 °C in an incubator with all the petri plates.

Using a UV-vis spectrophotometer (Systronics 2203, India), the photocatalytic activity includes F-NPs, G/F-NCs, Bi/F-NPs and G/Bi/F-NCs. In order to assess the breakdown of the dye under UV light, 0.9 mg L^{-1} of an aqueous solution of the generated catalysts was added to 8 mg L^{-1} of methylene blue (MB) dye concentration with a pH = 8.

3. The Results and Discussion

3.1 Structural Studies

In Figure 2, F-NP, G/F-NC, Bi/F-NP, and G/Bi/F-NC XRD patterns are displayed. The diffraction peaks of the F-NPs are indexed in the XRD pattern at 18.39° (111), 30.25° (220), 35.54° (311), 43.01° (400), 53.20° (422), 57.16° (511) and 62.86° (440). The diffraction peaks of G/F-NCs have an XRD pattern that is 30.41° (220), 35.47° (311), 43.23° (400), 53.37° (422), 56.97° (511) and 62.63° (440). The emergence of the graphene (002) peak in G/F-NCs is a sign that G/F-NCs nanocomposites have formed. The diffraction peaks of the XRD pattern of Bi/F-NPs are 18.31° (111), 30.09° (220), 35.02° (311), 42.11° (400), 52.28° (422), 56.75° (511) and 62.53° (440). When compared to pure F- NPs, the peaks with Bi doping were slightly displaced to lower angles, indicating that the Fe_3 and Fe_2 ions in the Fe_3O_4 lattice had been replaced by the ions of Bi. Due to the ease with which both iron and bismuth ions were able to occupy their favoured positions, Bi/F- NPs formation was the most advantageous. G/Bi/F-NCs have an XRD pattern is used to index the peaks at 30.21° (220), 35.15° (311), 42.55° (400), 53.15° (422), 56.45° (511) and 62.65° (440). In accordance with the (002) reflection of graphene, a small peak at 24.3° could be seen in the XRD pattern of G/Bi/F-NCs (Cheng et al., 2017). These findings suggest that the Fe_3O_4 crystal phase in the G/Bi/F-NCs was not altered by the addition of graphene. These are reflections of the Fe_3O_4 nanoparticles' Face Centred Cubic (FCC) structure taken from the JCPDS file No. 65-3107 (Anjana et al.,2018).

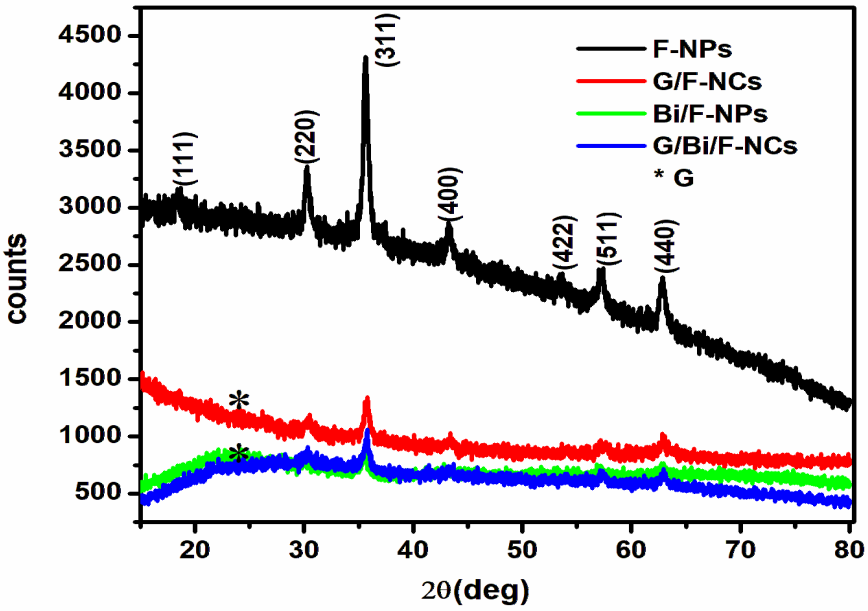

Figure 2 displays the X-ray diffraction F-NP, G/F-NC, Bi/F-NP and G/Bi/F-NC patterns

Table 1 lists bond length on the octahedral and tetrahedral sites of the cubic spinel structure, crystal size, cell volume, strain, lattice constant, and the dislocation density of F-NPs, G/F-NPs, Bi/F-NPs, and G/Bi/F-NCs. The approximate crystalline diameters were 34.22 nm, 38.61 nm, 42.24 nm, 39.51 nm, and 39.51 nm for F-NPs, G/F-NCs, Bi/F-NPs, and G/Bi/F-NCs, respectively, according to Scherrer's equation. In comparison to F-NPs, Bi/F-NPs offer bigger sizes based on calculated crystallite sizes. According to Karthikeyan et al. (2017), it showed that the Bi/F-NPs is highly crystalline and pure. This shows that the addition of Bi 4f can greatly accelerate the growth of the crystalline grains in F-NPs, as indicated by the fact that the crystalline size of Bi/F-NPs increased. The final lattice parameters were determined as 8.3880, 8.3845, 8.3820 and 8.3839 correspondingly, for F-NPS, G/F-NCs, Bi/F-NPs and G/Bi/F-NCs. They have a value of 8.396 which is much less than mass matter. This is due to the assembly of nanoparticles produced by internal atoms being compressed into spherical entities (Sun et al., 2006). Bi ions were substituted for Fe_3 and Fe_2 ions in the Fe_3O_4 lattice to improve the lattice characteristics since their ionic radius was higher (1.03) than theirs (0.75) and (0.69) (Arsalani et al., 2010).The measured lattice parameter and cell volume are in good agreement with the values in JCPDS file no. 65-3107 (a=8.390, V = 590.70 3). Due to its direct proportionality to lattice constant values (Somvanshi et al., 2020), the values of cell volume follow a pattern that is comparable to that of the lattice constant. The variation in the I220/I440 values can be used to describe the cations at the octahedral and tetrahedral positions (Lassoued et al., 2018).

Table 1: Table 1: Structural parameters of F-NPs, G/F-NCs, Bi/F-NPs and G/Bi/F-NCs

Sample	Grain size (D) (nm)	Lattice parameter (A°)	Dislocation density (δ) (m^{-2})	Cell volume (V) ($A°^3$)	Strain	Hopping length (L_A) (A°)	Hopping length (L_B) (A°)	X-ray density (d_x) (gm/cm^3)	Tetrahedral bond length (d_{AX}) (A°)	Octahedral bond length	Surface area (m^2/g)	Pore Volume (cm^3/g)	Pore size (nm)

										(d_{BX}) (A°)			
F-NPs	34.22	8.3880	0.00085	590.17	0.0087	3.6327	2.9660	5.2119	1.8161	2.097	48.742	0.168	13.766
G/F-NCs	38.61	8.3845	0.00069	589.43	0.00099	3.6322	2.9648	5.2185	1.8153	2.0961	69.798	0.126	7.197
Bi/F-NPs	42.24	8.3820	0.00056	580.17	0.00089	3.6305	2.9627	5.2919	1.8011	2.0915	63.832	0.162	10.170
G/Bi/F-NCs	39.51	8.3839	0.00064	584.57	0.0009	3.6310	2.9634	5.2734	1.8056	2.0922	90.847	0.260	11.445

The produced G/Bi/F-NCs' oxidation states are determined using X-ray photoelectron spectroscopy (XPS). The survey spectrum of G/Bi/F-NCs is shown in Fig.3(a), confirming the presence of bismuth, iron, and oxygen components in the finished product. Additionally, the presence of graphene in the manufactured material is what causes the carbon peak to occur. Elements found by XPS analysis in terms of their atomic percentage Fe is 27.12%, O is 46.97%, C is 25.61%, and Bi is 0.78%. According to the inset (Wu et al., 2015; Zhang et al., 2016), Fig. 3(b) of the high-resolution XPS spectra of Fe 2p shows two strong peaks brought on by $2p_{3/2}$ (at approximately 711.39 eV) and $2p_{1/2}$ (at approximately 725.21 eV). Fe^{2+} and Fe^{3+} ion-related peaks are present at 711.05 eV and 712.98 eV, respectively, according to the deconvolution of the $2p_{3/2}$ peak. In addition, the $2p_{1/2}$ peak's deconvolution reveals two peaks 725.54 eV and 732.73 eV brought on by Fe^{2+}.and Fe^{3+} ions that are present in the Fe_3O_4 lattice (Wang et al., 2012; Chen et al., 2013). According to Saurabh et al. (2019), the high-resolution Bi 4f XPS spectra (Fig. 3(c)) clearly consist of two deconvoluted peaks with binding energies of Bi $4f_{7/2}$ and Bi $4f_{5/2}$, respectively, 159.66 and 164.96 eV. Bi^{3+} oxidation state was indicated by the binding energy values of the Bi $4f_{7/2}$, which ranged from 159.66 eV to 160.82 eV (Alessio et al., 2018; Barrera et al., 2015; Xu et al., 2011). It was possible to deconvolute the high resolution C1s level XPS spectra (Fig. 3(d)) into four peaks. The sp^2 hybridised carbon present in graphene is responsible for the significant peak at 284.75 eV. According to Chang et al. (2013), the distinct surface oxidation states (C-O, C=O, and O-C=O, respectively) are responsible for the peaks at 285.54, 288.62, and 293.28 eV. Three peaks are detected in Fig. 3(e) shows the high-resolution O1s spectrum, with the strongest peak at 530.38 eV being assigned the Fe_3O_4 lattice's O anions. At 531.86 and 532.78 eV, the two peaks are caused by oxygen forming surface bonds with graphene in the composite and oxygen brought on by a Fe-OH group contaminating the Fe_3O_4 particle's surface, respectively. The spectra's high binding energy region may contain a large number of minor peaks that are mostly related to surface imperfections, impurities, and oxygen species were chemisorbed. However, as the spectra demonstrate , if they are present at all, they are not large enough to have a substantial impact on the current study (Wang et al., 2012).

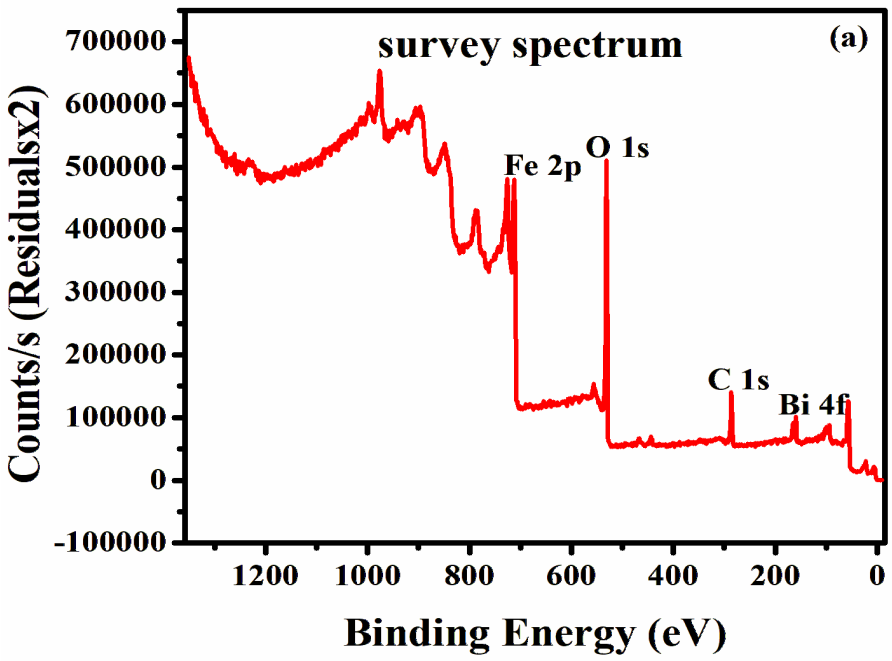
survey spectrum
(a)
Fe 2p
O 1s
C 1s
Bi 4f
Counts/s (Residualsx2)
Binding Energy (eV)

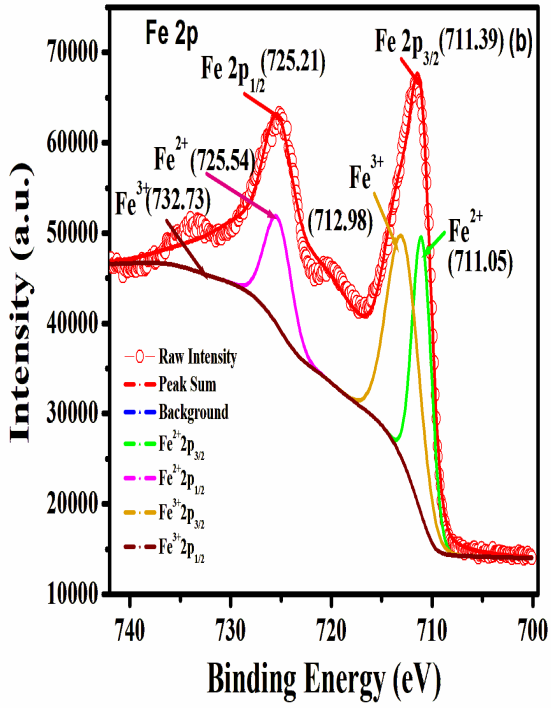
Fe 2p
Fe 2p1/2 (725.21)
Fe 2p3/2 (711.39) (b)
Fe2+ (725.54)
Fe3+ (732.73)
(712.98)
Fe3+
Fe2+ (711.05)
Raw Intensity
Peak Sum
Background
Intensity (a.u.)
Binding Energy (eV)

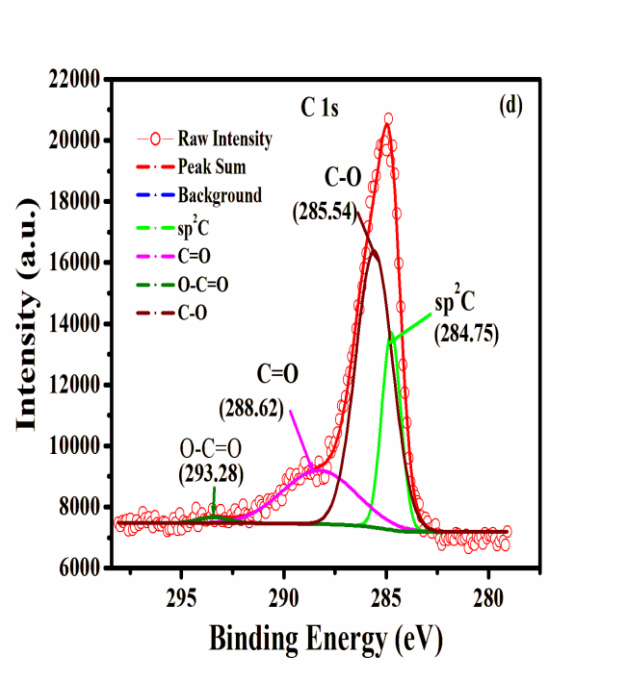
C 1s
(d)
Raw Intensity
Peak Sum
Background
sp2C
C=O
O-C=O
C-O
C-O
(285.54)
sp2C
(284.75)
C=O
(288.62)
O-C=O
(293.28)
Intensity (a.u.)
Binding Energy (eV)

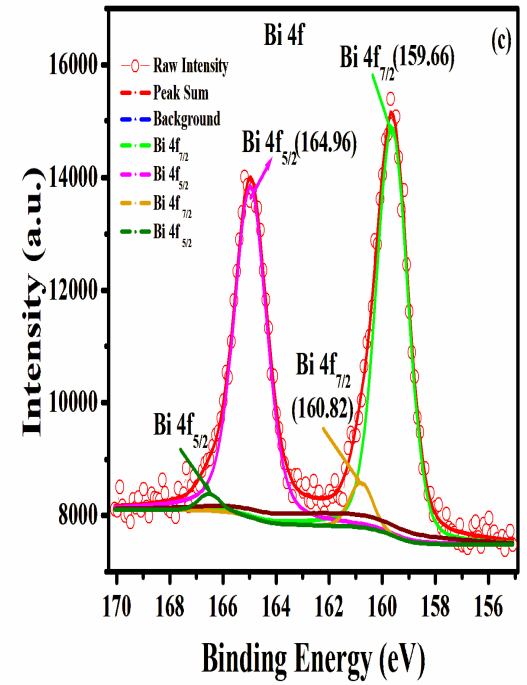
Bi 4f
(c)
Raw Intensity
Peak Sum
Background
Bi 4f7/2
Bi 4f5/2
Bi 4f7/2
Bi 4f5/2
Bi 4f7/2(159.66)
Bi 4f5/2(164.96)
Bi 4f7/2
(160.82)
Bi 4f5/2
Intensity (a.u.)
Binding Energy (eV)

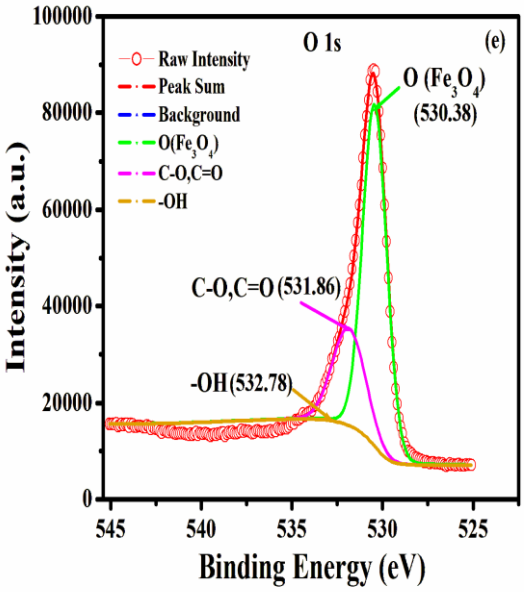

Fig.3 Synthesised G/Bi/F-NCs' XPS spectra: The survey spectrum, the Fe2p, the Bi 4f, the C 1s, and the O 1s spectra

3.2 Optical studies

The band gap energy plot and UV-vis absorption spectra of F-NPs, G/F-NCs, Bi/F-NPs, and G/Bi/F-NCs are shown in Figs. 4(a) and (b) for the purpose of analysing the optical absorption and band gap characteristics of these materials. F-NPs, Bi/F-NPs, G/F-NCs, and G/Bi/F-NCs all exhibited optical absorption at 400, 409, 405, and 407 nm, respectively. The optical band gaps of F-NPs, Bi/F-NPs, G/F-NCs, and G/Bi/F-NCs are displayed in Fig. 4(b) as 2.97, 2.51, 2.85, and 2.69 eV, respectively. According to Cabot et al. (2007), the band gap of bulk Fe_3O_4 is stated to be 0.1 eV, which is less than that of the produced nanocomposites. The bandgap is widened by the inclusion of Bi and G dopants. Anjana et al. (2018) reported that Zn-doped Fe_3O_4 nanoparticles and undoped Fe_3O_4 nanoparticles had bandgap values of 2.4 and 2.25 eV, respectively. Anjana et al. (2018) reported that the cobalt codoped Fe_3O_4 nanoparticles and rGO have bandgap values of 1.901 eV. The optical bandgaps of the rGO and nickel codoped Fe_3O_4 nanoparticles, also known as Fe_3O_4, Ni@Fe_3O_4, G@Fe_3O_4, and Ni/G@Fe_3O_4 (Sherin et al.,2023), were 1.970 eV, 1.824, 2.094, and 2.130 eV, respectively. It is common established that as particle size decreases, a substance's band gap energy increases (Manikandan et al., 2014; Ferraz et al., 2021). This bandgap energy fell as the particle size rose, and in the current instance (Bi doping), the optical absorption was redshifted. This could be explained by Bi and Fe have different electronegativity and ionic radiuses caused via formation of new defects structured as Fe atoms for Bi atoms. The system's higher disorder may be caused by the Bi 4f ions' larger ionic radius when contrasted with the ions of the base metal Fe_2. The bandgap energy reduction may have this as one of its possible causes. Reduced bandgap energy indicates that the bandgap decrease and absorption redshift are caused by sp-d spin-exchange interactions between the band electrons and localised d-electrons in the Bi dopants (Modwi et al., 2019). The acceptor energy level may fall below the conduction band or the donor energy could surpass the initial valence band, which would cause a reduction (Zhang et al., 2020). Bi may also induce additional impure energy in the prohibited band. The quantum confinement property of G/Bi/F-NCs is demonstrated by the high bandgap energy produced by the codoping of Bi and G into Fe_3O_4. The codopants absorbed smaller G/Bi/F-NCs more readily, which led to photocatalysis.

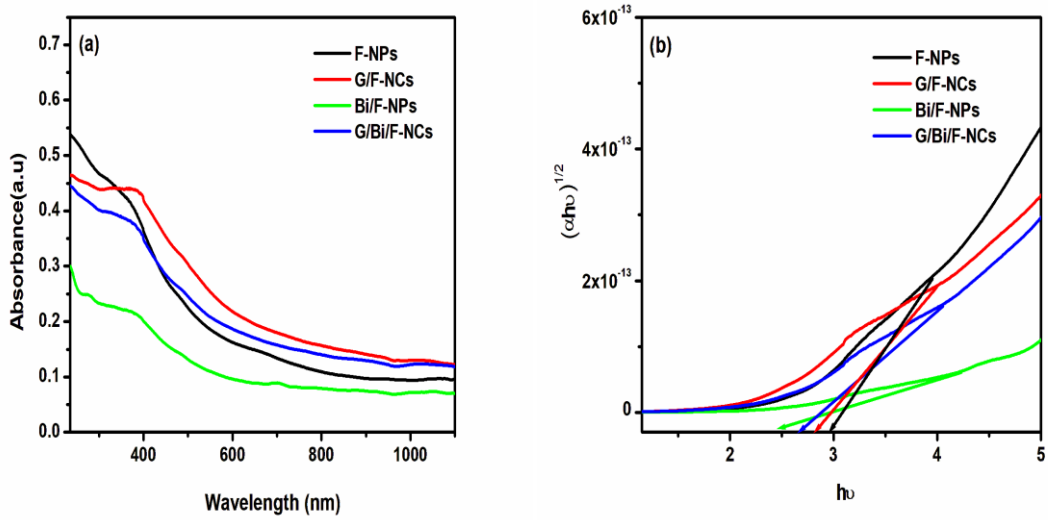

Figure 4 (a) shows the UV-vis spectra, and in (b), the band gaps of the F-NPs, G/F-NCs, Bi/F-NPs, and G/Bi/F-NCs are displayed.

Photoluminescence (PL) spectroscopy is used to further examine the produced nanoparticles' optical characteristics. The absorbance of F-NPs, G/F-NCs, Bi/F-NPs, and G/Bi/F-NCs stimulated at 340 nm is depicted in Fig. 4(c), and they exhibit PL from the visible to near infrared region, although with varying intensities and wavelengths. The F-NPs' absorption peaks are situated at 359.91, 492.05, 519.87, and 593.63 nm. We measured the G/F-NCs' absorption maxima at 362.06, 493.44, 521.24, and 592.85 nm. Bi/F-NPs exhibit absorption peaks at wavelengths of 361.38, 494.89, 535.84, and 596.38 nm. At 361.38, 495.58, 535.15, and 596.38 nm, the G/Bi/F-NCs' absorption peaks are visible. Bulk Fe_3O_4 doesn't, however, show any PL. This results from the various spatial configurations and particle confinement geometries. The high SA per unit mass of the nanoparticle in this case enhances surface activity and has a propensity to react with the hydroxide molecules of water adsorbed during the chemical reaction, which in this case explains the interactions on the nanoparticle surfaces. However, the Fe_3O_4's Fe^{2+} ions and water's oxygen molecules have a significant affinity for one another. By stimulating semiconductor materials with light, electrons and holes are produced. Fluorescence is produced when electrons and holes unite again. The separation rate of photoinduced charges was therefore examined using PL characterizations of F-NPS, Bi/F-NPs, G/F-NCs, and G/Bi/F-NCs. The difference between the PL intensities of G/Bi/F-NCs and F-NPs can be noted in Fig. 4(c). The F-NPs sample had a decreased rate of photogenerated charges recombining due to loaded Fe_3O_4 (Kexin et al., 2020). The transmission of charge at the interface between the dopants with the Fe_3O_4 is what causes the luminescence observed on bismuth and graphene doped Fe_3O_4. The presence of dopants results in a prominent, red-shifted excitonic emission peak because to collective emissions and light scattering. Compared to G/Bi/F-NCs and F-NPs, the higher absorbance with a red shift of the latter are the result of the dopants' formation of a chemical bond with Fe_3O_4 following the incorporation of graphene and bismuth (Fu et al., 2012; Phan et al., 2011).

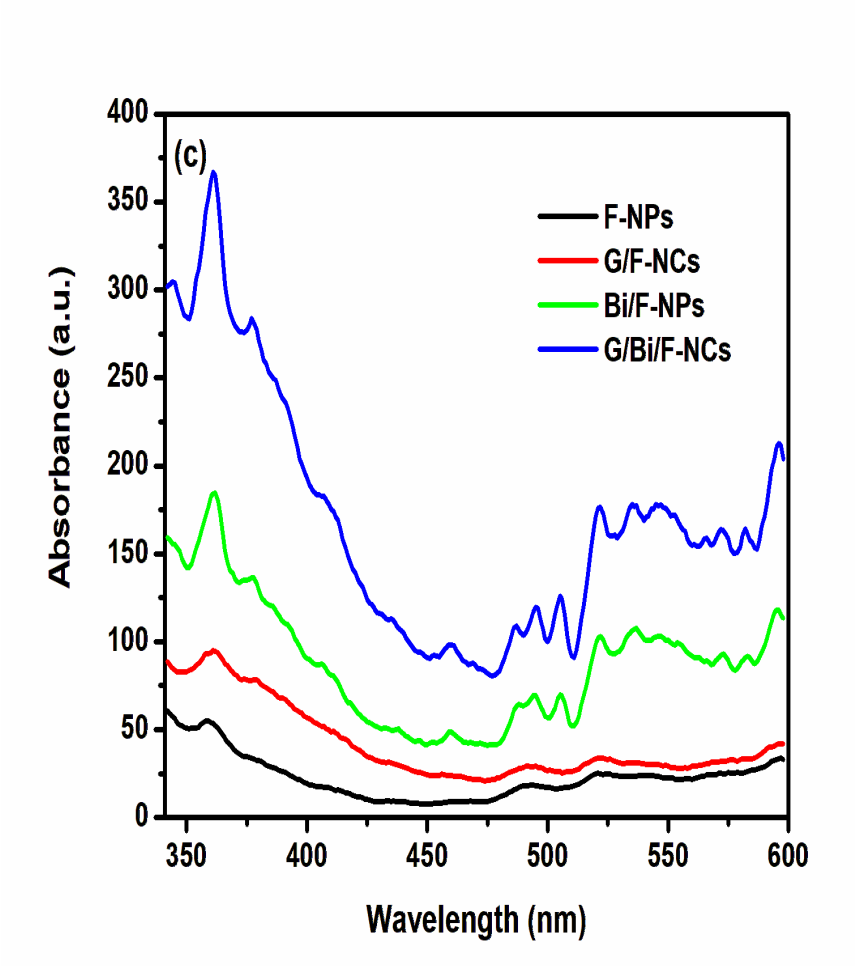

In Figure 4(c), the PL absorption spectra of F-NPs, G/F-NCs, Bi/F-NPs and G/Bi/F-NCs are displayed

3.3 Vibrational Studies

Fig. 5 displays F-NPs, G/F-NCs, Bi/F-NPs and G/Bi/F-NCs FTIR spectrum. Characteristic peaks were seen in the spectra at approximately 3437.29, 2921.03, 2878.49, 1635.19, 1391.51, 1197.40, 1041.83, 827.43, 544.84, and 447.10cm^{-1}. According to Haw et al. (2011), broad bands at 3437.29 cm-1 are related to water molecule O-H vibrations on the nanoparticle surfaces. According to Haw et al. (2011), the bands at 1635.19, 1391.51cm^{-1}, and 800.75 cm^{-1} correspond to the stretching vibrations of C=O, C-C, and C-H. G/Bi/F-NCs and G/F-NCs samples include graphene, which is confirmed by the presence of and C=O groups. According to these lowered vibrations, ions Fe^{3+} and Fe^{2+} from Fe_3O_4 lessen the tremors of the carbon bonding (Rezapour et al., 2018; Lyubutin et al., 2018; Sharma et al., 2017). The nanocomposite's the peaks are caused by C-N stretching vibration seen between 1235.95 and 915.17 cm^{-1} Liu et al. (2018). The FTIR spectrum of G/F-NCs shows a vibration signal at about 1157.47 cm^{-1} for the C-O stretching vibrations, which are proof that graphene and Fe_3O_4 nanoparticles have been integrated. The bands at 788.52, 544.84, and 447.10 cm^{-1} in the Fe-O stretching vibrations of the Fe^{2+} and Fe^{3+} ions in the octahedral and tetrahedral positions are represented in the FTIR spectra of the F-NPs, which supports the production of the Fe_3O_4 spinel structure (Agnihotri et al., 2020; Keiser et al., 1982). The bands at in the FTIR spectra of G/Bi/F-NCs are 788.52, 544.84 and 447.10 cm^{-1} are shifted towards 798.15, 564.11 and 456.73 cm^{-1}. Because the Fe^{2+} ions in the Fe_3O_4 lattice were replaced with Bi ions, the band was shifting attributed upto the bond length substitution (Yang et al., 2009). The FTIR data shows that bismuth ions were successfully incorporated into the Fe_3O_4 lattice in G/Bi/F-NCs.

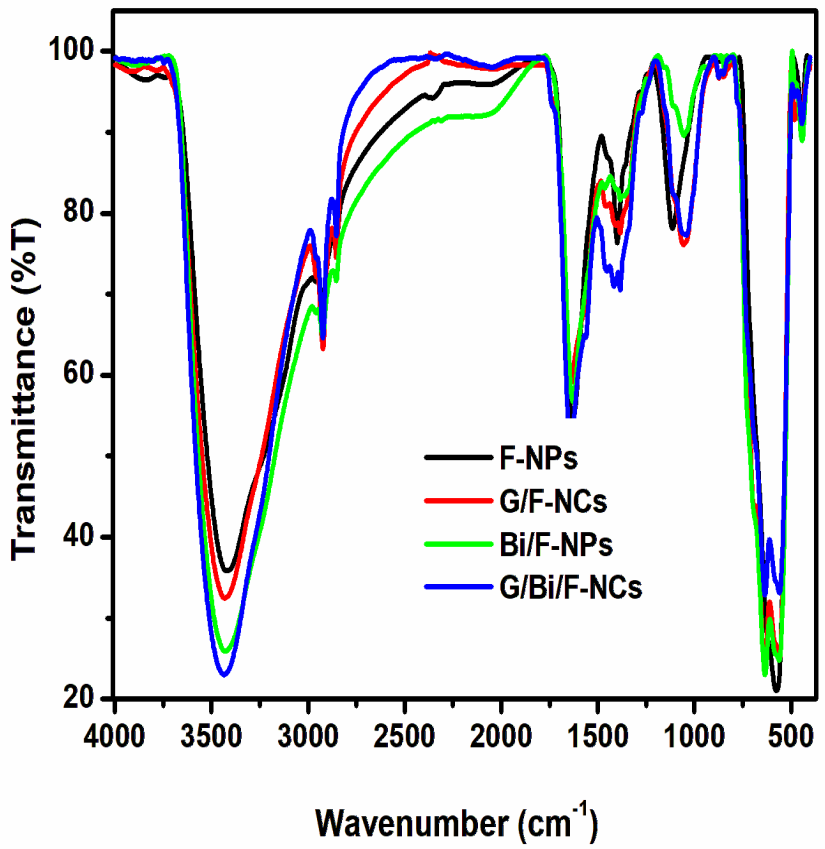

Figure 5 displays the FT-IR spectra of F-NPs, G/F-NCs, Bi/F-NPs, and G/Bi/F-NCs

3.4 Morphological studies

The surface morphology of synthetic F-NPs, G/F-NCs, Bi/F-NPs, and G/Bi/F-NCs is shown in Figures 6(a, b, c and d). We find that the resultant nanoparticles have a spherical form. Using EDAX measurement, the synthesised F-NPs, G/F-NCs, Bi/F-NPs and G/Bi/F-NCs' elemental configuration is examined. The results are shown in Fig. 6 (e, f, g and h). Iron signals are present in the EDAX spectra of all samples (F-NPs, G/F-NCs, Bi/F-NPs, and G/Bi/F-NCs). At 0.5 keV, the oxygen signal is seen, confirming that oxygen exists in the synthesised nanoparticles. The formation of Fe_3O_4 nanoparticles is supported by the prominent Fe and O peaks in the EDAX spectra. The carbon peak at 0.3 keV in spectra of G/F-NCs and G/Bi/F-NCs in EDAX indicates the existence of graphene in the synthesised material. According to Mishra et al. (2016), Figure 6(h) of the EDAX spectra of G/Bi/F-NCs displays signals for bismuth at 2.45 and 10.83keV, supporting the presence of Bi in the Fe_3O_4 nanoparticles. Table 2, Supporting Information, summarizes the atomic percentages of the elements detected through EDAX analysis.

(a) (b) (c) (d)

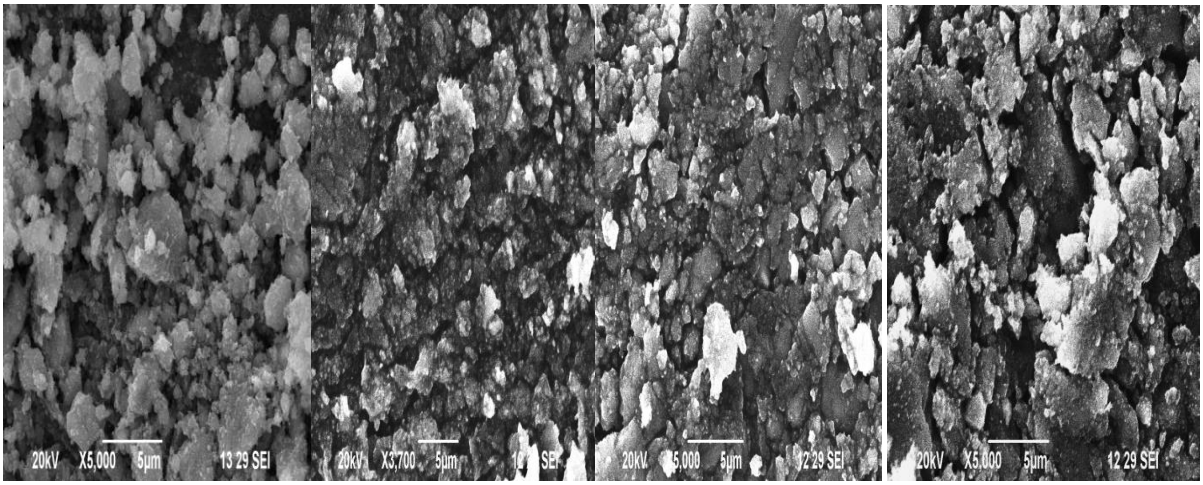

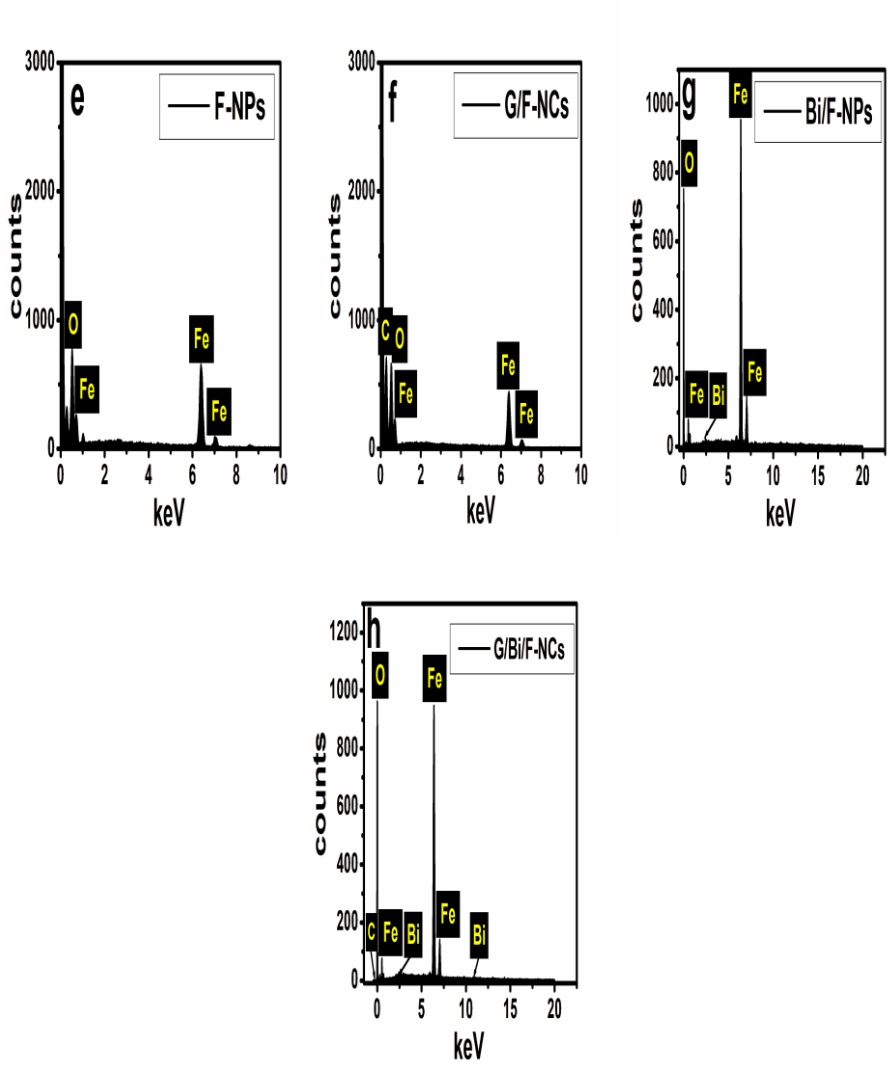

Figure 6 shows SEM pictures of F-NPs, G/F-NCs, Bi/F-NPs and G/Bi/F-NCs together with EDAX spectra of each of these materials

Table.2 Atomic percentage of elements detected by EDX analysis

Samples/Element	Fe		O		C		Bi	
	(wt.%)	(at.%)	(wt.%)	(at.%)	(wt.%)	(at.%)	(wt.%)	(at.%)
F-NPs	60.48	30.48	39.52	69.52	-	-	-	-
G/F-NCs	22.55	6.69	39.54	40.98	37.91	52.33	-	-
Bi/F-NPs	86.46	70.68	10.00	28.54			3.54	0.77
G/Bi/F-NCs	82.49	57.82	8.92	21.82	6.10	19.89	2.48	0.46

The microstructure of the samples of F-NPs, G/F-NCs, Bi/F-NPs and G/Bi/F-NCs after TEM investigation is shown in Figure 7(a), (b), (c) and (d). The produced Fe_3O_4 nanoparticles are crystallised, as shown in Fig. 7. Fe_3O_4 nanoparticles are scattered over the surface of graphene, as observed in Figure 7(b and d), which shows TEM pictures. For F-NPs and Bi/F-NPs, the computed average particle size is 35.72 nm and 42.78 nm, respectively. Additionally, the average particle sizes both G/F-NCs and G/Bi/F-NCs include F-NPs have been determined to be 39.14 nm and 40.25 nm, correspondingly. The slight rise bringing average particle size in response to the chemical reaction's aggregation of graphene. The typical crystal size estimated using XRD data is rather close to this value. Iron oxide nanoparticle particle dispersion becomes more spherical and homogeneous with the addition of C and Bi. Figure 7(e, f, g and h) shows the SAED pattern of F-NPs, G/F-NCs, Bi/F-NPs, and G/Bi/F-NCs. Since the production of iron oxide nanoparticles, all F-NPs, G/F-NCs, Bi/F-NPs, and G/Bi/F-NCs exhibit rings associated with the (111), (220), (311), (400), (422), (511) and (440) planes. All SAED patterns are seen to be quite intense, which shows that nanoscale particles are being produced. As a result, the SAED pattern indicates the presence of Fe_3O_4 nanoparticles in their pure form due to the lack of any additional iron salts (Sun et al., 2011).

(a) **(b)** **(c)** **(d)**

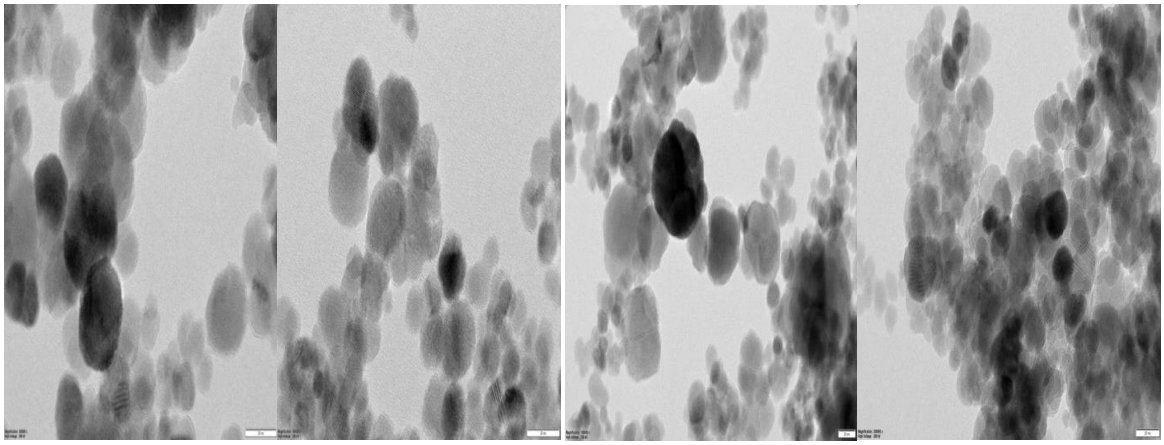

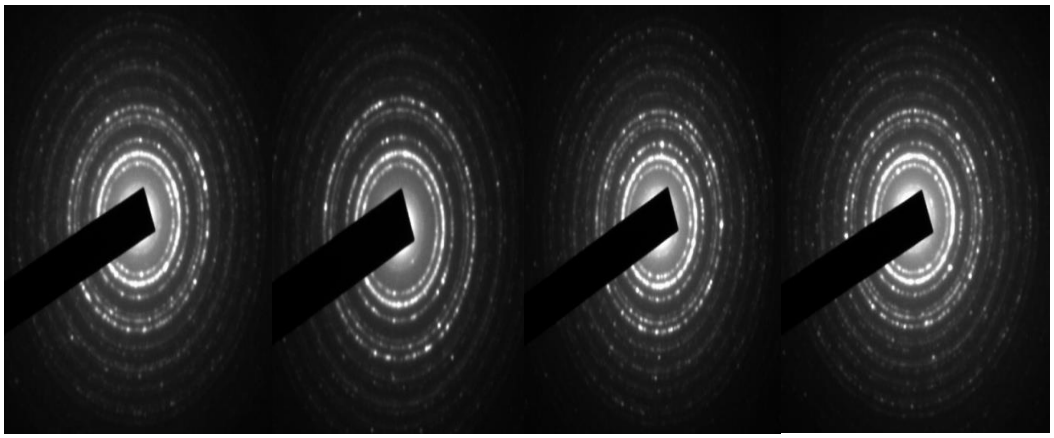

(e) (f) (g) (h)

Figure 7 shows TEM images of (a) F-NPs, (b) G/F-NCs, (c) Bi/F-NPs and (d) G/Bi/F-NCs, along with e) F-NPs, f) G/F-NCs, g) Bi/F-NPs and h) G/Bi/F-NCs SAED patterns

3.5 BET surface area analysis

In Fig. 8, the nitrogen-adsorption and -desorption isotherms F-NPs, G/F-NCs, Bi/F-NPs, and G/Bi/F-NCs from the samples are depicted. Table 1 lists the surface areas, pore volumes, and pore diameters of the produced materials. In the range of 0.4 to 1 relative pressures, the isotherms show clear hysteresis loops, confirming mesoporous nanocomposites' presence. The surface areas of F-NPs, G/F-NCs, Bi/F-NPs, and G/Bi/F-NCs were computed using the Brunauer-Emmett-Teller (BET) method and were found to be 48.742, 69.798, 63.832 and 90.847 m^2/g, respectively. Following Bi and G doping, the samples' surface areas rose, which is explained by a reduction in the crystalline size of the Fe_3O_4 nanoparticles. G/Bi/F-NCs' enhanced specific surface area is due to the addition of graphene nanoflakes and the development of secondary pores (Su et al.,2011; Lian et al.,2010; Chen et al.,2011). The system with the greatest amount of G/Bi/F-NCs surface area has been chosen for future research on the adsorption of MB from wastewater since it is suitable for adsorption applications (Aashima et al.,2019).

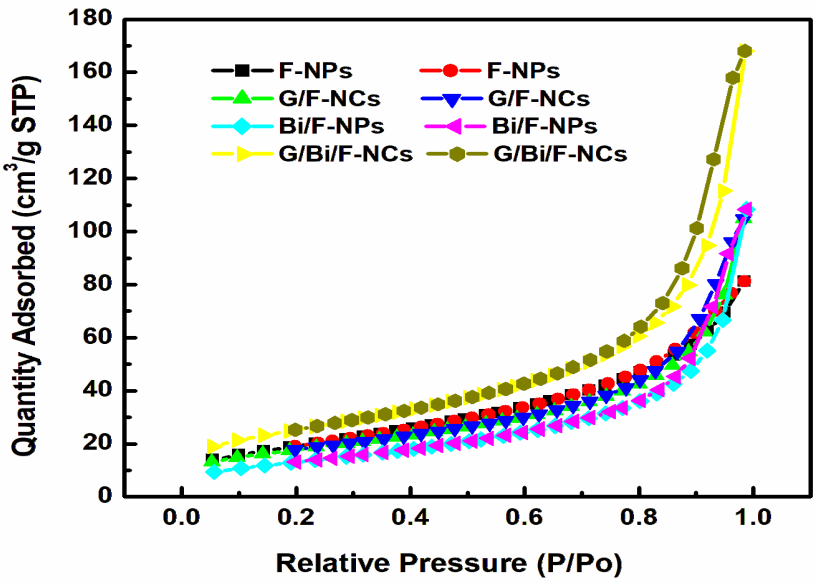

Figure 8. Nitrogen Adsorption and Desorption Isotherms for G/F-NCs, Bi/F-NPs, F-NPs, and G/Bi/F-NCs

3.6 Antimicrobial activities of F-NPs, G/F-NCs, Bi/F-NPs and G/Bi/F-NCs

Staphylococcus aureus spreads and causes a number of dangerous infections; it is effectively kept in hospital implants (Ribeiro et al., 2012). A ubiquitous environmental bacterium called Pseudomonas aeruginosa has the ability to infect people, causing a variety of deadly infections both acute and chronic, particularly in those with compromised immune systems (Qin et al., 2022). One of the main causes of the rise in death rates is the introduction of drug-resistant bacteria. Therefore, it is strongly advised to discover and identify new methods for creating drugs that work well against these bacterial types. The antibacterial properties include G/F-NCs, G/Bi/F-NCs, F-NPs, and Bi/F-NPs against a range of dangerous bacteria, including the often seen water-borne gram-positive pathogen S. aureus and gram-negative pathogen P. aeruginosa, and fungus, Aspergillus flavus, were investigated using the disc diffusion method (Figure 9 and dates are tabulated in Table 3). As shown in Fig. 9, the produced nanoparticles showed a ZOI of 18 and 15 mm for P. aeruginosa and A. flavus, respectively, whereas S. aureus had a 19 mm maximum area of inhibition.

Due to modifications in the structure of their cell walls, the bacteria Staphylococcus aureus were shown to be more vulnerable to chemical stressors than the other two species. S. aureus's cell membrane reacts to nanoparticles when it comes into contact with them, allowing additional metal ions to get through. As a result, S. aureus experiences cell death and becomes less vulnerable to drugs. Due to graphene's toxicity, oxidative stress, and electron transfer, the G/Bi/F-NCs nanocomposites have a significant antibacterial activity (Kumar et al., 2019). By coming into contact with its sharp edges, it can directly harm the bacterial membranes. Reactive oxygen species (ROS) formed by graphene include superoxide and hydroxyl radicals, singlet oxygen, and hydrogen peroxide allow bacteria to reproduce by inactivating their lipids and proteins (Kumar et al., 2019). It serves as an electron (es) acceptor and removes es from the membrane, perhaps improving the membrane's integrity (Kumar et al., 2019). The Fenton reaction produces ROS, which results in lipid peroxidation, DNA damage, and protein oxidation. ROS can kill bacteria without harming nonbacterial creatures. The ROS production's bactericidal effect was exerted on both positive and negative microorganisms. Kim et al. claim that hydrogen peroxide was created when Fe_2 reacted with oxygen. Hydroxyl radicals can harm biological molecules when the resultant hydrogen peroxide undergoes the Fenton reaction with ferrous ions (Kumar et al., 2019).

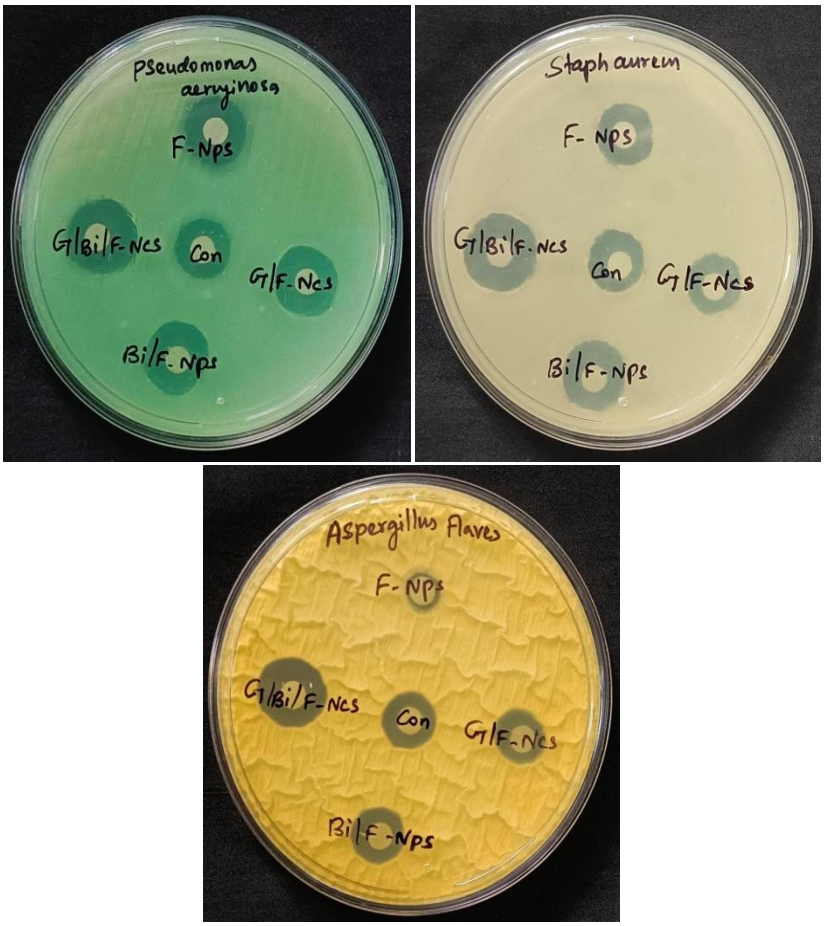

Figure 9 demonstrates the ZOI for the F-NPs, G/F-NCs, Bi/F-NPs and G/Bi/F-NCs for Pseudomonas aeruginosa, Staph aureus, and Aspergillus flaves

Table 3 ZOI of F-NPs, G/F-NCs, Bi/F-NPs and G/Bi/F-NCs

	F-NPs	G/F-NCs	Bi/F-NPs	G/Bi/F-NCs	Control (Amikacin)
Pseudomonas aeruginosa	11 mm	13 mm	14 mm	18mm	10 mm
Staph aureus	13 mm	16 mm	17 mm	19mm	12 mm
					Control (Nystatin)
Aspergillus Flaves	9 mm	11 mm	13 mm	15mm	14mm

3.7 Photocatalytic Degradation of F-NPs, G/F-NCs, Bi/F-NPs and G/Bi/F-NCs

Because it converts hazardous contaminants into tiny, inorganic molecules (like CO_2 and H_2O), photocatalytic degradation is one of the most essential and effective strategies to disinfect industrial waste water using light irradiation (Arefeh et al., 2019; Su shiung et al., 2020). Industrial dyeing wastes are toxic and non-biodegradable, as well as having an adverse effect on the environment. Methylene blue (MB), a phenothiazine derivative used in the textile dyeing process, is exceedingly toxic and carcinogenic. In this study, we looked at the photocatalytic degradation of aqueous MB brought on by UV light irradiation at different time intervals while

using nanocatalysts that were created (F-NPs, G/F-NCs, Bi/F-NPs and G/Bi/F-NCs). The photocatalytic degradation of MB over F-NPs, G/F-NCs, Bi/F-NPs, and G/Bi/F-NCs is shown in Figure 10(a-d). With 330 minutes of exposure, it demonstrated a stepwise drop in the intensity of MB absorption at 661 nm, confirming that MB is degraded by adsorption on the surface of the produced nanocatalysts.

Photons can be efficiently absorbed due to the UV region of nanocomposite's great absorption. From graphene's valence band to conduction band, the electrons on the surface of Fe_3O_4 are transported. These trapped electrons produce O_2 (super oxide radical) on the surface of graphene, which confers electron hole separation. During the reduction procedure, the sp^2 hybridization was restored, which resulted in the larger electronic conductivity of graphene, which in turn controlled the recombination of electron-hole pairs in Fe_3O_4. The electron-hole pairs are responsible for the redox interaction between the catalyst and MB molecules (Hisatomi et al., 2014; Hoffmann et al., 1995). The hydroxyl free radical (active ingredient) is created when the Fe_3O_4 holes (photo-generated) incorporate with OH, water and MB dye. Both the conduction band's ability to decrease atomic and the surface of the nanoparticles exhibits positive hydroxyl radical production capability of the valence band.The hydroxyl radicals produced have an oxidising effect on the G/Bi/F-NCs' surface-administered organic dyes.

$$Fe_3O_4 + H\nu \rightarrow h^+_{vb} + e^-_{cb}$$

$$(O_2)_{ads} + e^-_{cb} \rightarrow {}^{\cdot}O_2^-$$

$$H_2O + h^+ \rightarrow H^+ + OH^{\cdot}$$

Although they no longer participate in oxidation, super oxide radicals still interact with H^+ to produce $HO_2^{\cdot}$. As a result, (Active spices) are created as hydroxyl free radicals when $HO_2^{\cdot}$ reacts with water or dyes and has more trapped e^- at the valence band. These radicals are created on the surface of photocatalysts by the photocatalytic oxidation of water and reduction of oxygen (Behnam et al., 2021).

$${}^{\cdot}H^+ + O_2^- \rightarrow HO_2^{\cdot}$$

$$e^- + HO_2^{\cdot} \rightarrow OH^{\cdot}$$

As a result, the radicals ${}^{\cdot}O_2$, $HO_2^{\cdot}$, and $OH^{\cdot}$ degrade MB into CO_2 and H_2O as degradation byproducts.

$$OH^{\cdot} / HO_2^{\cdot} / O_2^- + MB \rightarrow \text{Degradation Products } (CO_2 + H_2O)$$

It was discovered that F-NPs, G/F-NCs, Bi/F-NPs, and G/Bi/F-NCs contributed within 330 minutes of irradiation 62%, 71%, 54% and 86% of MB pollutant degradation, respectively. In contrast to F-NPs, G/F-NCs and Bi/F-NPs, G/Bi/F-NCs had a higher degrading efficiency. According to Asha et al., 2021; Bessy et al., 2022; Ancy et al., 2021; and Bindhu et al., 2021, the rate constant (kapp) of this catalytic process was determined using a pseudo-first-order kinetic equation. Fig. 10(e) shows a linear plot of ln (At/A0) with time. The values of k_{app} are given for F-NPs, G/F-NCs, Bi/F-NPs, and G/Bi/F-NCs were 0.005, 0.007, 0.002, and 0.012/min. G/Bi/F-NCs have a higher predicted k_{app} value because of their high adsorption capacity (caused by the abundance of high photoactivity is the result of both the presence of more active sites for the adsorption of MB molecules on their surface and great light diffusion. Due to graphene's high surface area and superior electrical conductivity, G/Bi/F-NCs can enhance photocatalytic activity. This encourages the interaction of the dye molecules with the catalyst through electron transfer, hydroxyl radicals, and reactive sites. According to Hoffman et al. (1995), the MB's thiazine ring serves as a photocatalyst sensitizer and is more vulnerable to photoreduction.

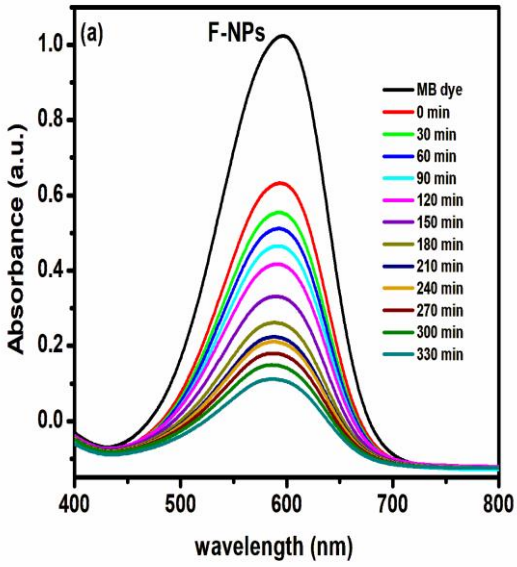
(a)
F-NPs
Absorbance (a.u.)
wavelength (nm)
MB dye
0 min
30 min
60 min
90 min
120 min
150 min
180 min
210 min
240 min
270 min
300 min
330 min

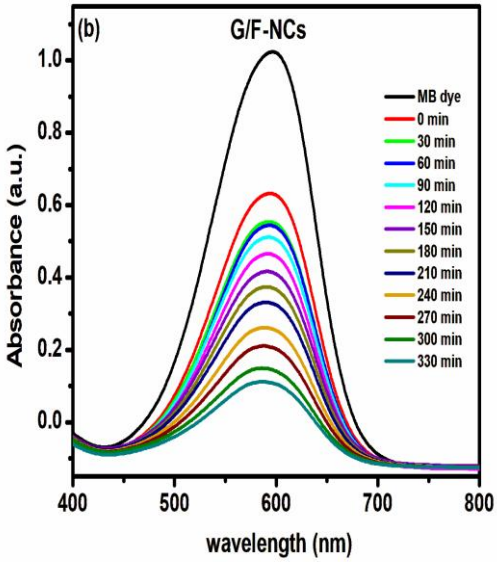
(b)
G/F-NCs
Absorbance (a.u.)
wavelength (nm)
MB dye
0 min
30 min
60 min
90 min
120 min
150 min
180 min
210 min
240 min
270 min
300 min
330 min

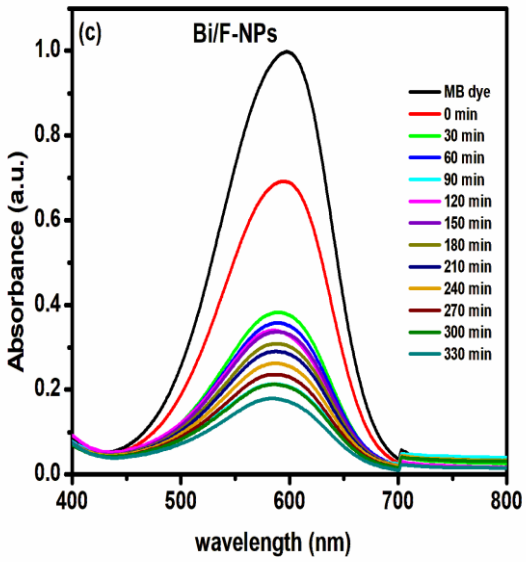
(c)
Bi/F-NPs
Absorbance (a.u.)
wavelength (nm)
MB dye
0 min
30 min
60 min
90 min
120 min
150 min
180 min
210 min
240 min
270 min
300 min
330 min

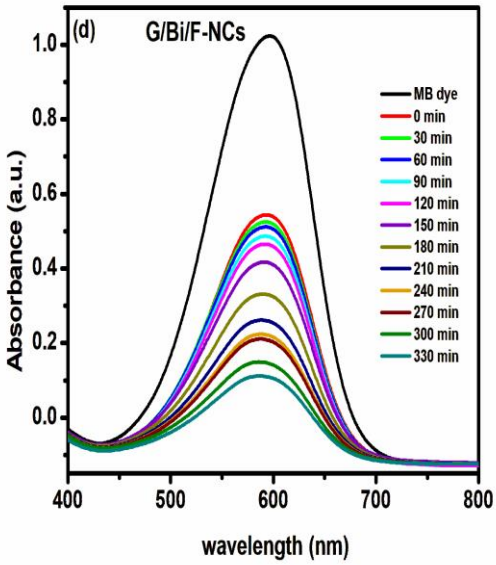
(d)
G/Bi/F-NCs
Absorbance (a.u.)
wavelength (nm)
MB dye
0 min
30 min
60 min
90 min
120 min
150 min
180 min
210 min
240 min
270 min
300 min
330 min

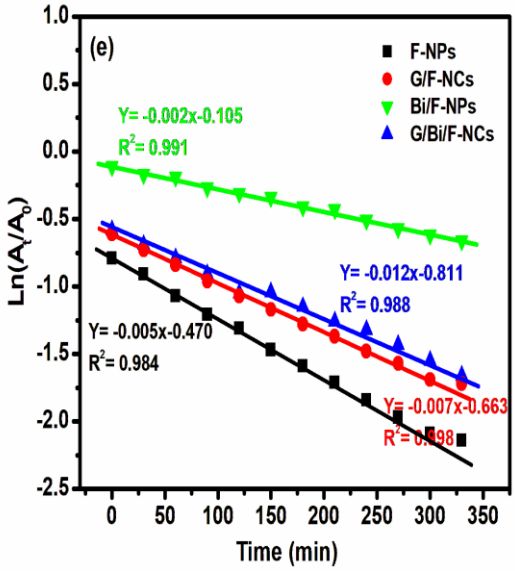
(e)
F-NPs
G/F-NCs
Bi/F-NPs
G/Bi/F-NCs
Y= -0.002x-0.105
R2= 0.991
Y= -0.012x-0.811
R2= 0.988
Y= -0.005x-0.470
R2= 0.984
Y= -0.007x-0.663
Ln(At/A0)
Time (min)

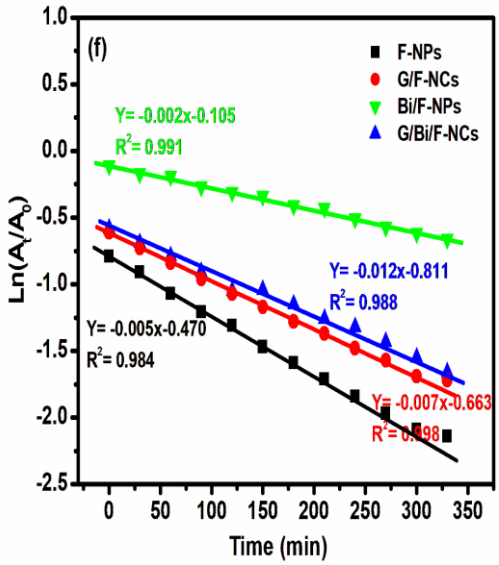
(f)
F-NPs
G/F-NCs
Bi/F-NPs
G/Bi/F-NCs
Y= -0.002x-0.105
R2= 0.991
Y= -0.012x-0.811
R2= 0.988
Y= -0.005x-0.470
R2= 0.984
Y= -0.007x-0.663
Ln(At/A0)
Time (min)

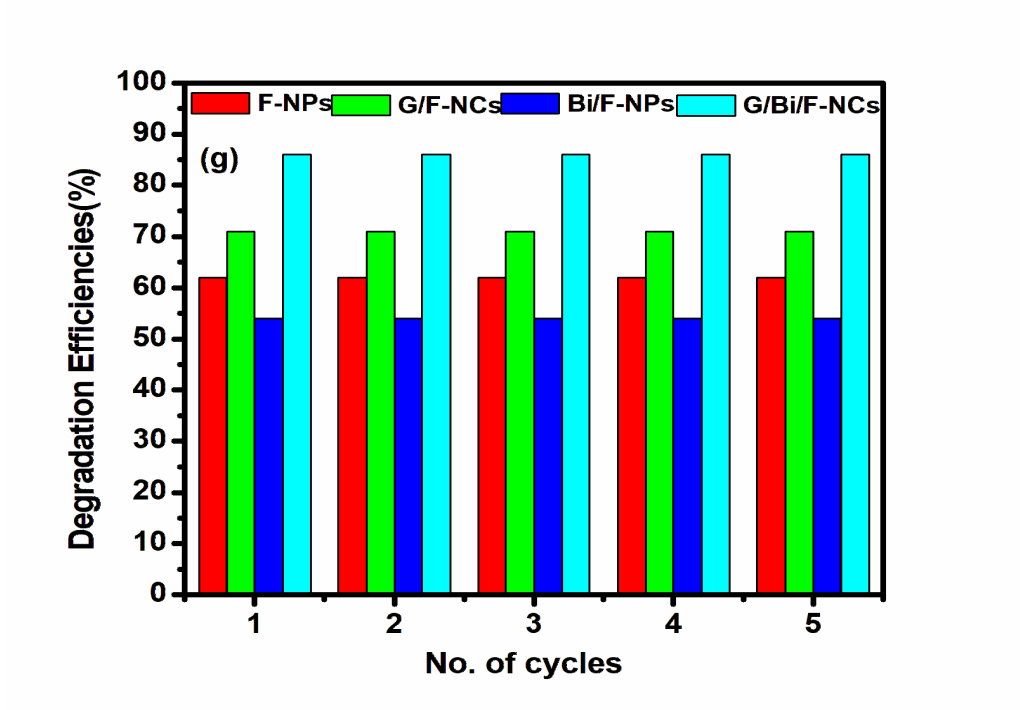

Photocatalytic degradation curves for MB are shown in Fig. 10(a-d), along with a linear plot of Ln (At/A0) versus reaction time in (e), a linear plot of Ln (At/A0) versus reaction time after seven days in (f), and a plot of degradation (%) versus cycle count for F-NPs, G/F-NCs, Bi/F-NPs and G/Bi/F-NCs

The great stability towards the photocatalytic process of F-NPs, G/F-NCs, Bi/F-NPs and G/Bi/F-NCs is demonstrated by the observation of no discernible changes in their rate constant values even after 7 days (Fig. 10(f)). From the reaction mixture, all of the produced photocatalysts are separated using centrifugation. This experiment is run five times using photocatalysts for a comparable reaction time of 330 minutes after being cleaned with water. No discernible changes in the degradation efficiencies are seen (Fig.10(g)). The samples calcined at 300°C because of this. This might be clearing out any contaminants that could turn off the photocatalyst. The regenerated photocatalysts (F-NPs, G/F-NCs, Bi/F-NPs, and G/Bi/F-NCs) were found to have stable catalytic activity confirmed the noteworthy reutilization for the degradation of MB. The schematic diagram of the G/Bi/F-NCs' role in the degradation of MB dye is shown in Fig. 11.

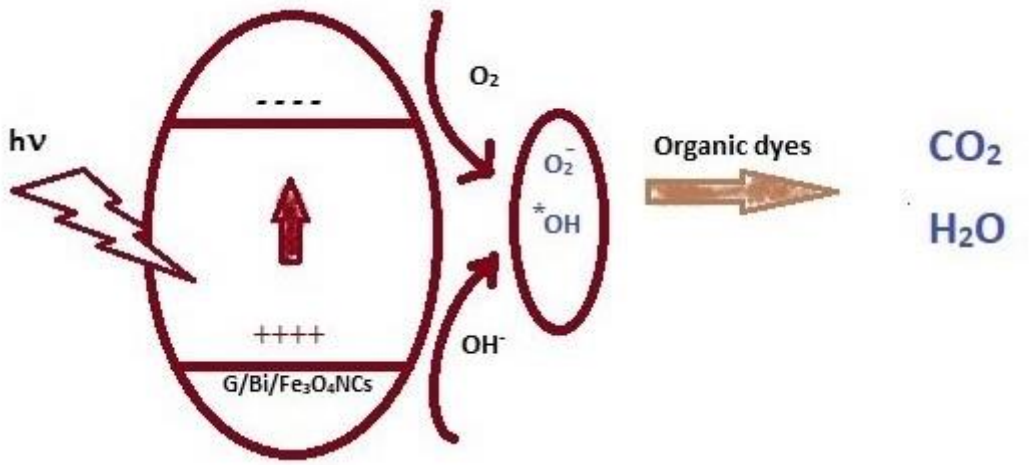

Figure 11 shows a schematic representation of the process by which G/Bi/F-NCs degrade MB dye.

4. Conclusion

The photocatalytic and antibacterial properties of undoped, single-element doped, and codoped Fe_3O_4 nanocomposites (F-NPs, G/F-NPs, Bi/F-NPs and G/Bi/F-NCs) were studied in order to compare the degradation of industrial dyes. The integration of G and Bi 4f ions into Fe_3O_4 was successfully demonstrated by the XRD, XPS, FTIR, and EDAX results. Scherrer's equation determined that the approximate crystallite sizes of F-NPs, G/F-NCs, Bi/F-NPs and G/Bi/F-NCs were 34.22 nm, 38.61 nm, 42.24 nm, and 39.51 nm, respectively. F-NPs, Bi/F-NPs, G/F-NCs and G/Bi/F-NCs exhibited optical bandgap of 2.97, 2.51, 2.85, and 2.69 eV, respectively. The BET surface areas of F-NPs, G/F-NCs, Bi/F-NPs, and G/Bi/F-NCs were calculated to be 48.742, 63.832, 51.632, and 90.847 m^2/g, respectively. The k_{app} values were calculated as 0.005, 0.007, 0.002 and 0.012/min for F-NPs, G/F-NCs, Bi/F-NPs, and G/Bi/F-NCs, respectively. The expected k_{app} value was larger due to G/Bi/F-NCs' high photoactivity and considerable capacity for light absorption. The produced nanoparticles had a maximum ZOI of 19 mm when tested against S. aureus. The double dopant integration raised the specific surface area and increased electron conduction between materials to improve the electrical conductivity, catalytic performance, and antibacterial capabilities of the composite. We showed that nanocomposites comprising graphene and bismuth are likely to improve the binding of nanoparticles to bacteria.

5. List of abbreviations

Fe_3O_4	iron oxide nanoparticles
Bi	Bismuth
G	Graphene
F-NPs	nanoparticles of Fe_3O_4
G/F- NCs	Graphene-doped nanocomposites of Fe_3O_4
G/Bi/F-NCs	Iron oxide nanocomposites co-doped with bismuth and graphene
XRD	X-ray diffraction
XPS	X-Ray Photoelectron spectroscopy
FTIR	Fourier transform - infra red spectroscopy
UV-vis	UV-visible Spectroscopy
PL	photoluminescence spectroscopy
TEM	Transmission electron microscopy
SEM	Scanning electron microscopy
EDAX	Energy dispersive
SAED	Selected area electron diffraction
BET	Brunauer Emmett Teller
ZOI	Zone of Inhibition
ROS	Reactive Oxygen Species
DNA	Deoxyribonucleic Acid
MB	Methylene blue
k_{app}	Rate constant

References

1. Aashima, Shivani Uppal, Arushi Arora, Sanjeev Gautam, Suman Singh, Choudharyd R. J and Mehta S. K. Magnetically retrievable Ce-doped Fe_3O_4 nanoparticles as scaffolds for the removal of azo dyes. RSC Adv., 2019, 9, 23129. DOI: 10.1039/c9ra03252e.
2. Aftabtalab, A. and Sadabadi, H., "Application of magnetite (Fe_3O_4) nanoparticles in hexavalent chromium adsorption from aquatic solutions", Journal of Petroleum & Environmental Biotechnology, Vol. 6, No. 200, (2015), 1–6.
3. Agnihotri, P., Lad, V.N., 2020. Magnetic nanofluid: synthesis and characterization. Chem. Pap. 74, 3089–3100. https://doi.org/10.1007/s11696-020-01138-w.
4. Agusu, L., Alimin, Ahmad, L. O., Firihu, M. Z., Mitsudo, S., and Kikuchi, H. (2019). Crystal and Microstructure of $MnFe_2O_4$ Synthesized by Ceramic Method Using Manganese Ore and Iron Sand as Raw Material. Journal of Physics, 1-8.
5. Alessio Verni, G.; Long, B.; Gity, F.; Lanius, M.; Schüffelgen, P.; Mussler, G.; Grützmacher, D.; Greer, J.; Holmes, J.D. Oxide removal and stabilization of bismuth thin films through chemically bound thiol layers. Rsc Adv. 2018, 8, 33368–33373.
6. Al-Farhan, B. S., "Removal of Cd and Pb Ions from Aqueous Solutions Using Bentonite-Modified Magnetic Nanoparticles", International Journal of Nano Dimension, Vol. 2, No. 1, (2016), 27–31.
7. Amara D., Felner I., Nowik I., Margel S., Synthesis and characterization of Fe and Fe_3O_4 nanoparticles by thermal decomposition of triiron dodecacarbony, Colloids Surf., A 339 (2009) 106-110.
8. Ancy, K., Vijilvani, C., Bindhu, M.R., Jeslin Sunitha Bai, S., Khalid, S.A., Turki, M.D., Ayman, M., Mohammed, S.A., 2021. Visible light assisted photocatalytic degradation of commercial dyes and waste water by Sn–F co-doped titanium dioxide nanoparticles with potential antimicrobial application. Chemosphere, 277, 130247. https://doi.org/10.1016/j.chemosphere.2021.130247.
9. Anjana P. M., Joe Sherin J. F., Vijayakumar C., Sarath Kumar S. R., Bindhu M. R., Rakhi R. B., Mater. Sci. Eng. B 2023, 290, 116313.
10. Anjana, P.M., Bindhu, M.R., Umadevi, M., Rakhi, R.B., 2018. Antimicrobial, electrochemical and photo catalytic activities of Zn doped Fe_3O_4 nanoparticles. J. Mater. Sci. Mater. Elect. 29, 6040-6050. https://doi.org/10.1007/s10854-018- 8578-2.
11. Arakha, M., Pal, S., Samantarrai, D., Panigrahi, T.K., Mallick, B.C., Pramanik, K., Mallick, B.,Jha, S., 2015. Antimicrobial activity of iron oxide nanoparticle upon modulation of nanoparticle-bacteria interface. Sci. Rep. 5(1), 14813. https://doi.org/10.1038/srep14813.
12. Arefeh Ahadi, Hassan Alamgholiloo, Sadegh Rostamnia, Xiao Liu, Mohammadreza Shokouhimehr, Diego A. Alonso, Rafael Luque, Layer-Wise Titania Growth Within Dimeric Organic Functional Group Viologen Periodic Mesoporous Organosilica as Efficient Photocatalyst for Oxidative Formic Acid Decomposition. The European Soceity Journal for Catalysis, 2019. 11(19) p. 4803-4809. https://doi.org/10.1002/cctc.201900486.
13. Arsalani N., Fattahi H., Nazarpoor M., Express Polym. Lett. 2010, 4, 329.
14. Asha, S., Hentry, C., Bindhu, M.R., Al-Mohaimeed, A.M., AbdelGawwad, M.R., Elshikh, M.S., 2021. Improved photocatalytic activity for degradation of textile dyeing waste water and thiazine dyes using $PbWO_4$ nanoparticles synthesized by coprecipitation method. Environ. Res.200,111721. https://doi.org/10.1016/j.envres.2021.111721.
15. Ashraf, M.; Shah, S.S.; Khan, I.; Aziz, M.A.; Ullah, N.; Khan, M.; Adil, S.F.; Liaqat, Z.; Usman, M.; Tremel, W.; et al. A HighPerformance Asymmetric Supercapacitor Based on Tungsten Oxide Nanoplates and Highly Reduced Graphene Oxide Electrodes. Chem. Eur. J. 2021, in press.
16. Athar, T., 2015. Smart precursors for smart nanoparticles. Emerging Nanotechnologies for Manufacturing (Second Edition). Micro and Nano Tech. 444-538. https://doi.org/10.1016/B978-0-323-28990-0.00017-8.
17. Bala, D. A., Ali, H., Eli, D. and Yunana, T. "Optical Properties of Reduced Graphene Oxide on Iron Oxide Nanoparticles", Vol. 3 No. 2, June, 2019, pp 226-231.

18. Balamurugan, J.; Nguyen, T. T.; Aravindan, V.; Kim, N. H.; Lee, J., Flexible Solid-State Asymmetric Supercapacitors Based on Nitrogen-Doped Graphene Encapsulated Ternary Metal-Nitrides with Ultralong Cycle Life. Advanced Functional Materials 2018, 28. http://dx.doi.org/10.1002/adfm.201804663.
19. Balamurugan, J.; Nguyen, T. T.; Aravindan, V.; Kim, N. H.; Lee, S. H.; Lee, J. H., All ternary metal selenide nanostructures for high energy flexible charge storage devices. Nano Energy 2019, 65, 10 https://doi.org/10.1016/j.nanoen.2019.103999.
20. Balamurugan, J.; Thanh, T. D.; Kim, N. H.; Lee, J. H., Facile synthesis of 3D hierarchical Ndoped graphene nanosheet/cobalt encapsulated carbon nanotubes for high energy density asymmetric supercapacitors. Journal of Materials Chemistry A 2016, 4 (24), 9555-9565. https://doi.org/10.1039/C6TA03132C.
21. Barrera-Mota, K.; Bizarro, M.; Castellino, M.; Tagliaferro, A.; Hernández, A.; Rodil, S.E. Spray deposited β-Bi_2O_3 nanostructured films with visible photocatalytic activity for solar water treatment. Photochem. Photobiol. Sci. 2015, 14, 1110–1119.
22. BehnamNayebi, Kasra Pourrostami Niavol, Behzad Nayebi, Soo Young Kim, Ki Tae Nam, Ho Won Jang, Rajender S. Varma and Mohammadreza Shokouhimehr, Prussian blue-based nanostructured materials: Catalytic applications for environmental remediation and energy conversion. Molecular Catalysis, 2021. 514. p. 111835. https://doi.org/10.1016/j.mcat.2021.111835.
23. Beji, Z., Hanini, A., Smiri, L. S., Gavard, J., Kacem, K., Villain, F., et al. (2010). Magnetic properties of Zn-Substituted $MnFe_2O_4$ Nanoparticles Synthesized in Polyol as Potential Heating Agents for Hyperthermia. Evaluation of Their Toxicity on Endhothelial Cells. Chemistry of Materials, 5420-5429.
24. Bessy, T.C., Bindhu, M.R., Johnson, J., Chen, S.-M., Chen, T.-W., Almaary, K. S., 2022. UV light assisted photocatalytic degradation of textile waste water by Mg0.8- xZnxFe_2O_4 synthesized by combustion method and in-vitro antimicrobial activities. Environ. Res. 111917. https://doi.org/10.1016/j.envres.2021.111917.
25. Bharath, G.; Hai, A.; Kiruthiga, T.; Rambabu, K.; Sabri, M. A.; Park, J.; Choi, M. Y.; Banat, F.; Haija, M. A., Fabrication of Ru–$CoFe_2O_4$/RGO hierarchical nanostructures for high-performance photoelectrodes to reduce hazards Cr(VI) into Cr(III) coupled with anodic oxidation of phenols. Chemosphere 2022, 13443. https://doi.org/10.1016/j.chemosphere.2022.134439.
26. Bindhu, M.R., Willington, T.D., Hatshan, M.R., Chen, S.-M., Chen, T.-W., 2021. Environmental photochemistry with Sn/F simultaneously doped TiO_2 nanoparticles: UV and visible light induced degradation of thiazine dye. Environ. Res. 112108. https://doi.org/10.1016/j.envres.2021.112108.
27. Cabot, A., Puntes, V. F., Shevchenko, E., Yin, Y., Balcells, L., Marcus, M. A., Hughes, S.M., Alivisatos, A.P., 2007. Vacancy Coalescence during Oxidation of Iron Nanoparticles. J. American Chem. Soc. 129(34), 10358-10360. http://doi.org/10.1021/ja072574a.
28. Cao, W., Ma, Y., Zhou, W. and Guo, L., "One-pot hydrothermal synthesis of
29. Chandra, V., Park, J., Chun, Y., Lee, J.W., Hwang, I.C., Kim, K.S., 2010. Waterdispersible magnetite-reduced graphene oxide composites for arsenic removal. ACS Nano 4, 3979e3986. http://dx.doi.org/10.1021/nn1008897.
30. Chang Y. C and Chen D. H., J. Colloid Interface Sci., 283, 446-451 (2005).
31. Chang, Y., Li, J., Wang, B., Luo, H., He, H., Song, Q., Zhi, L., 2013. Synthesis of 3D nitrogen-doped graphene/Fe_3O_4 by a metal ion induced self-assembly process for high-performance Li-ion batteries. J. Mater. Chem. A, 1(46), 14658-14665. http://doi.org/10.1039/c3ta13370b.
32. Chen D. Y., Ji G., Ma Y., Lee J. Y., Lu J. M., ACS Appl. Mater. Interfaces 2011, 3, 3078.
33. Chen H. I. and Chang H. Y.: Colloid Surface A, 2005, 242, 61-69.
34. Chen, R., Chen, R., Chai, L., Li, Q., Shi, Y., Wang, Y., Mohammad, A., 2013. Preparation and characterization of magnetic Fe_3O_4/CNT nanoparticles by RPO method to enhance the efficient removal of Cr(VI). Environ. Sci. Pollut. Res. Int. 20(10), 7175-85. http://doi.org/10.1007/s11356-013-1671-4.
35. Chen, Y., Fu, X.-Y., Yue, Y.-Y., Zhang, N., Feng, J., Sun, H.-B., 2019. Flexible and transparent supercapacitor based on ultrathin Au/graphene composite electrodes. Applied Surface Sci. 467-468 104-111. http://doi.org/:10.1016/j.apsusc.2018.10.093.

36. Cheng Q. D., Gong S., Zhang Q., Wang R., Jiang L., J. Mater. Chem. A 2017, 5, 16386.
37. Chimezie, A.B., Hajian, R., Yusof, N.A., Woi, P.M. and Shams, N., "Fabrication of reduced graphene oxide-magnetic nanocomposite (rGO-Fe_3O_4) as an electrochemical sensor for trace determination of As (III) in water resources", Journal of Electroanalytical Chemistry, Vol. 796, (2017), 33–42.
38. Chin, A.B., Yaacob, I.I., 2007. Synthesis and characterization of magnetic iron oxide nanoparticles via w/o microemulsion and Massart's procedure. J. Mater. Processing Tech. 191(1), 235-237. https://doi.org/10.1016/j.jmatprotec.2007.03.011.
39. Chou, C. Y.; Kuo, P.C.; Yao, Y.D.; Sun, A. C.; Fang, Y.H.; Chen, S. C.; Huang, C. H.; Chen, J. W. Effects of Sintering Temperature on the Magnetoresistance and Microstructure of the Mixture of Fe_3O_4 and Cu-Ferrite Powder. IEEE Trans. Magn. 2005, 41, 2757-2759.
40. Cruz, I. F., Freire, C., Araújo, J. P., Pereira, C., Pereira, A. M., 2018. Multifunctional Ferrite Nanoparticles: From Current Trends Toward the Future. Magnetic Nanostructured Mater. 59-116. http://doi.org/10.1016/b978-0-12-813904-2.00003-6.
41. Cui, H., Yang, W., Li, X., Zhao, H. and Yuan, Z., "An electrochemical sensor based on a magnetic Fe_3O_4 nanoparticles and gold nanoparticles modified electrode for sensitive determination of trace amounts of arsenic (III)", Analytical Methods, Vol. 4, No. 12, (2012), 4176–4181.
42. Cunqing Ma, Kaiyu yang, Lili Wang, Xin Wang. Facile synthesis of reduced graphene oxide/Fe_3O_4 nanocomposite film. J Appl Biomater Funct Mater 2017; 15(Suppl 1):S1-S6. DOI: 10.5301/jabfm.5000341.
43. Deng H., Li X. L., Peng Q., Wang X., Chen J. P., Li Y. D., Monodisperse magnetic single-crystal ferrite microspheres, Angew. Chem. Int. Ed. 44 (2005) 2782-2785.
44. Dubus S., Gravel J. F., Drogoff B. L., Nobert P., Veres T and Boudreau D, Anal. Chem., 78, 4457-4464 (2006).
45. Ferraz I. S. B., Castro T. J., Mantilla J., Coaquira J. A. H., Garg V. K., Oliveira A. C., Franco Jr A., Morais P. C., da Silva S. W., J. Alloys Compd. 2021, 887, 161398.
46. Gade N.E., Dar R.M., Mishra O.P., Khan J.R., Kumar V., and Patyal A.: Evaluation of dose-dependent cytotoxic effects of graphene oxide-iron oxide nanocomposite on caprine Wharton's jelly derived mesenchymal stem cells. J. Anim. Res. 5, 415 (2015).
47. Gautam, S., Shandilya, P., Priya, B., Singh, V. P., Raizada, P., Rai, R., et al. (2017). Superparamagnetic $MnFe_2O_4$ Dispersed over Graphitic Carbon Sand Composite and Bentonite as Magnetically Recoverable Photocatalyst for Antibiotic Mineralization. Seperation and Purification Technology, 498-511.
48. Geim A.K., Novoselov, K.S. 2007. The rise of graphene. Nature Mater.6, 183-191.
49. Giraldo, L., Erto, A and Moreno-Piraján, J. C., "Magnetite nanoparticles for removal of heavy metals from aqueous solutions: synthesis and characterization", Adsorption, Vol. 19, No. 2–4, (2013), 465–474.
50. Green wood, Norman N, Earnshaw, Alan. Chemistry of the Elements (2nd ed.). Butterworth-Heinemann.1997; ISBN 978-0-08-037941-8.
51. Gupta, S.S., Sreeprasad, T.S., Maliyekkal, S.M., Das, S.K., Pradeep, T., 2012. Graphene from sugar and its application in water purification. ACS Appl. Mater. Interfaces 4156e4163. http://dx.doi.org/10.1021/am300889u.
52. Gurunathan S., Woong Han J., Eppakayala V., and Kim J.: Green synthesis of graphene and its cytotoxic effects in human breast cancer cells. Int. J. Nanomed. 8, 1015 (2013).
53. Han, Q., Wang, Z., Xia, J., Chen, S., Zhang, X., Ding, M., Talanta 2012, 101, 388–395.
54. Hastak V., Bandi S., Kashyap S., Singh S., Luqman S., Lodhe M., Peshwe D.R., and Srivastav A.K.: Antioxidant efficacy of chitosan/ graphene functionalized superparamagnetic iron oxide nanoparticles. J. Mater. Sci.: Mater. Med. 29, 154 (2018).
55. Haw, C.Y., Chia, C.H., Zakaria, S., Mohamed, F., Radiman, S., Teh, C.H., Khiew P.S., Chiu W.S., Huang, N.M., 2011. Morphological studies of randomized dispersion magnetite nanoclusters coated with silica. Ceramint. 37(2), 451-464. http://doi.org/10.1016/j.ceramint.2010.09.010.

56. He, Z.; Koza, J. A.; Mu, G. J.; Miller, A. S.; Bohannan, E. w.; switzer, J. A. Electrodeposition of $Co_xFe_{3-x}O_4$ Epitaxial Films and Superlattices. Chem. Mater. 2013, 25, 223-232.
57. Hisatomi, T., Kubota, J., Domen, K., 2014. Recent advances in semiconductors for photocatalytic and photoelectrochemical water splitting. Chem. Soc. Rev. 43(22), 7520–7535. http://doi.org/10.1039/c3cs60378d.
58. Hoffmann, M.R., Martin, S.T., Choi, W., Bahnemann, D.W., 1995. Environmental Applications of Semiconductor Photocatalysis. Chem. Rev. 95(1), 69– 96. http://doi.org/10.1021/cr00033a004.
59. Hong R. Y., Pan T. T and Li H. Z., J. Magn. Magn. Mater., 303, 60-68 (2006).
60. Hosseini, S.H., Asadnia, A., 2013. Polyaniline/Fe_3O_4 coated on $MnFe_2O_4$ nanocomposite: Preparation, characterization, and applications in microwave absorption. J. Inter. Physical Sci. 8(22), 1209-1217. http://doi.org/10.5897/IJPS12.576.
61. Hu C. Q., Gao Z. H and Yang X. R, Chem. Phys. Lett., 429, 513-517 (2006).
62. Hu F. Q., Li Z., Tu C. F and Gao M. Y., J. Colloid Interface Sci., 311 (2007)469-474.
63. Jalil, Z., Rahwanto, A., Mustanir, Akhyar and Handoko, E. (2017). Magnetic Behaviour of Natural Magnetite (Fe_3O_4) Extracted from Beach Sand Obtained by Mechanical Alloying Method. AIP Conference Proceeding 1862 (pp. 030023-1-030023-4). Depok: AIP Publishing.
64. Jedrzejczak-Silicka M.: Cytotoxicity and genotoxicity of GO– Fe_3O_4 hybrid in cultured mammalian cells. Pol. J. Chem. Technol. 19, 27 (2017).
65. Joe Sherin J. F., Vijayakumar C., Bindhu M. R., Mansour K. Gatasheh, Ashraf Atef Hatamleh and Selvaraj Arokiyara, Phys. Status Solidi A 2023, 220, 2300076.
66. Jones H. The theory of the galvomagnetic effects in bismuth. Proceedings of the Royal Society of London. Series A: Mathematical and Physical Sciences. 1936;155(886):653-663. DOI: 10.1098/rspa.1936.0126.
67. Karim, M. R.; Mohammad, A.; Cho, M. H.; Yoon, T., Synergistic performance of Fe_3O_4/SnO_2/rGO nanocomposite for supercapacitor and visible light-responsive photocatalysis. International Journal of Energy Research 2022, 46 (5), 65 https://doi.org/10.1002/er.7588.
68. Karthikeyan K. & Thirumoorthi A., "Synthesis, Characterization and Photoluminescence Behaviour of Bismuth Ferrites", International Journal of Applied and Advanced Scientific Research, Volume 2, Issue 1, Page Number 51-56, 2017.
69. Keiser, J.T., Brown, C.W., Heidersbach, R.H., 1982. The Electrochemical Reduction of Rust Films on Weathering Steel Surfaces. J. Electrochem. Soc. 129(12), 2686. http://doi.org/10.1149/1.2123648.
70. Kexin Fang, Lei Shi, Lizhu Yao, Lishuang Cui. Synthesis of novel magnetically separable $Fe_3O_4/Bi_{12}O_{17}Cl_2$ photocatalyst with boosted visible-light photocatalytic activity. 129(2020)110888.
71. Khaghani S, Ghanbari D, Khaghani S. Green synthesis of iron oxide-palladium nanocomposites by pepper extract and its application in removing of Colored pollutants from water. Journal of Nanostructures. 2017;7(3):175-182.
72. Kim E. H., Lee H. S., Kwak B. K and Kim B. K, J. Magn. Mater., 289, 328-330 (2005).
73. Kim, D. H., Nikles, D.E., and Brazel, C. S. (2010). Synthesis and Characterization of Multifunctional Chitosan-$MnFe_2O_4$ Nanoparticles for Magnetic Hyperthermia and Drug Delivery. Materials, 4051-4065.
74. Kumar P., Huo P., Zhang R., Liu B., Nanomaterials 2019, 9, 737
75. Lassoued A., Lassoued M. S., García-Granda S., Dkhil B., Ammar S., Gadri A., J. Mater. Sci. 2018, 29, 5726
76. Laurent S., Forge D., Port M., Roch A., Robic C., Vander Elst L., Muller R.N., Magnetic iron oxide nanoparticles: synthesis, stabilization, vectorization, physico-chemical characterizations, and biological applications, Chem. Rev. 108 (2008) 2064-2011.
77. Laurent, S.; Forge, D.; Port, M.; Roch, A.; Robic, C.; Elst, L. V.; Muller, R. N. Chem. Rev. 2008, 108, 2064.

78. Lazarevic, Z. Z., Jovalekic, C., Milutinovic, A., Sekulic, D., Ivanoski, V. N., and Recnik, A. (2013). Nanodimensional Spinel $NiFe_2O_4$ and $ZnFe_2O_4$ Ferrites Prepared by soft Mechanochemical Synthesis. Journal of Applied Physics, 1-11.
79. Lee J W, Kim J D. In Situ Chemical Synthesis of Fe_3O_4 Nanoparticles on Reduced Graphene Oxide Sheets in Polyol Medium and Magnetic Properties[J]. Journal of nanoscience and nanotechnology, 2015, 15/1: 215-219.
80. Li Y. X., Zhou X. Z., Wang Y and You X.Z.: Mater. Lett., 2004, 58, 245-249.
81. Lian P. C., Zhu X. F., Xiang H. F., Li Z., Yang W. S., Wang H. H., Electrochim. Acta 2010, 56, 834.
82. Liang JJ, Xu YF, Sui D, et al. Flexible, magnetic and electrically conductive graphene/Fe_3O_4 paper and its application for magnetic controlled switches. J Phys Chem C. 2010;114(41):17465-17471.
83. Liang, C., Song, J., Zhang, Y., Guo, Y., Deng, M., Gao, W., Zhang, J., 2020. Facile Approach to Prepare rGO@Fe_3O_4 Microspheres for the Magnetically Targeted and NIRresponsive Chemo-photothermal Combination Therapy. Nanoscale Res. Lett. 15(1), 86. http://doi.org/10.1186/s11671-020-03320-1.
84. Lin, L., Liu, Y., Zhao, X., Li, J. H., Anal. Chem. 2011, 83, 8396-8402.
85. Liu MM, Sun J. In situ growth of monodisperse Fe_3O_4 nanoparticles on graphene as flexible paper for supercapacitor. Journal of Materials Chemistry A. 2014;2(30):12068-12074.
86. Liu, L.; Zhu, X.; Zeng, Y.; Wang, H.; Lu, Y.; Zhang, J.; Yin, Z.-Z.; Chen, Z.; Yang, Y.; Li, L., An Electrochemical Sensor for Diphenylamine Detection Based on Reduced Graphene Oxide/Fe_3O_4-Molecularly Imprinted Polymer with 1,4-Butanediyl-3,3'- bis-l-vinylimidazolium Dihexafluorophosphate Ionic Liquid as Cross-Linker. Polymers 2018, 10, 13. http://dx.doi.org/10.3390/polym10121329.
87. Liu, S.; Yu, B.; Wang, S.; Shen, Y.; Cong, H., Preparation, surface functionalization and application of Fe_3O_4 magnetic nanoparticles. Advances in Colloid and Interface Science 2020, 281, 10216. https://doi.org/10.1016/j.cis.2020.102165.
88. Liu, Y.; Wang, W.; Xu, X.; Marcel Veder, J.-P.; Shao, Z., Recent advances in anion-doped metal oxides for catalytic applications. Journal of Materials Chemistry A 2019, 7 (13), 7280-7300. https://doi.org/10.1039/C8TA09913H.
89. Lu, A.-H.; Salabas, E. L.; Schuth, F. Angew. Chem., Int. Ed. 2007, 46, 1222.
90. Lyubutin, I.S., Baskakov, A.O., Starchikov, S.S., Shih, K.-Y., Lin, C.-R., Tseng, Y.-T., Yang, S.-S., Han, Z.-Y., Ogarkova, Yu.L., Nikolaichik, V.I., Avilov, A.S., 2018. Synthesis and characterization of graphene modified by iron oxide nanoparticles. Mater. Chem. Phy. 219, 411-420. http://doi.org/10.1016/j.matchemphys.2018.08.042.
91. Mahalingam, S. and Ahn, Y. H., "Improved visible light photocatalytic activity of rGO–Fe_3O_4–NiO hybrid nanocomposites synthesized by in situ facile method for industrial wastewater treatment applications", New Journal of Chemistry, Vol. 42, No. 6, (2018), 4372–4383.
92. Mahdavi M., Namvar F., Ahmad M. B and Mohamad R., Molecules, 18, 5954(2013) DOI: 10.3390/molecules 18055954.
93. Maity, D., Agrawal, D.C., 2007. Synthesis of iron oxide nanoparticles under oxidizing environment and their stabilization in aqueous and non-aqueous media. J. Magnetism and Magnetic Mater. 308(1), 46-55. http://doi.org/10.1016/j.jmmm.2006.05.001.
94. Mandal, P., Chattopadhyay, A.P., 2015. Excellent catalytic activity of magnetically recoverable Fe_3O_4–graphene oxide nanocomposites prepared by a simple method. Dalton Trans. 44(25), 11444-11456. http://doi.org/10.1039/c5dt01260k.
95. Manikandan A., Vijaya J. J., Mary J. A., Kennedy L. J., Dinesh A., J. Ind. Eng. Chem. 2014, 20, 2077.
96. Mary Eagleson. Concise encyclopedia chemistry. Walter de Gruyter.1994; ISBN 3-11-011451-8.
97. Matijevic E., sapieszko R.S., Melville J.B., Ferric hydrous oxide sols I. Monodispersed basic iron(III) sulfate particles, J. Colloid Interface Sci. 50 (1975) 567-581.

98. Mishra, A., Mohanty, T., 2016. Structural and morphological study of magnetic Fe_3O_4/ reduced graphene oxide nanocomposites. Materials Today: Proceedings 3(6), 1576-1581. https://doi.org/10.1016/j.matpr.2016.04.045.
99. Modwi A., Khezami L., Taha K. K., Bessadok A., Mokraoui S., J. Mater. Sci. Mater. Electron. 2019, 30, 14714.
100. Moradinasab, S. and Behzad, M., "Removal of heavy metals from aqueous solution using Fe_3O_4 nanoparticles coated with Schiff base ligand", Desalination and Water Treatment, Vol. 57, No. 9, (2016), 4028–4036.
101. Moyer, J. A.; Vaz, C. A. F.; Negusse, E.; Arena, D. A.; Henrich, V. E. Controlling the Electronic Structure of Co_{1-x} $Fe_{2+x}O_4$ Thin Films through Iron Doping. Phys. Rev. B 2011, 83, 035121.
102. Mussa, Y.; Ahmed, F.; Arsalan, M.; Alsharaeh, E. Two dimensional (2D) reduced graphene oxide (RGO)/hexagonal boron nitride (h-BN) based nanocomposites as anodes for high temperature rechargeable lithium-ion batteries. Sci. Rep. 2020, 10(1), 1-13, https://doi.org/10.1038/s41598-020-58439-z.
103. Namvari, M. and Namazi, H., "Clicking graphene oxide and Fe_3O_4 nanoparticles together: an efficient adsorbent to remove dyes from aqueous solutions", International Journal of Environmental Science and Technology, Vol. 11, No. 6, (2014), 1527–1536.
104. Naseri, M. G., Saion, E. B., Ahangar, H. A., Hashim, M., and Shaari, A. H. (2011). Synthesis and Characterization of Manganese Ferrite Nanoparticles by Thermal Treatment Method. Journal of Magnetism and Magnetic Material, 1745- 1749.
105. Nayamadi Mahmoodabadi A., Kompany A., Mashreghi M., Mater. Chem. Phys. 2018, 213, 285.
106. Ng, W.C., Tan C.Y., Ong, B.H., Matsuda, A. Procedia Eng., 2017, 184, 587-594.
107. Novoselov K. S., Geim A. K., Morozov S. V., Jiang D., Zhang Y., Dubonos S. V., Grigorieva I. V., Firsov A. A., Science 2004, 306, 666.
108. Ou J, Wang F, Huang Y, et al. Fabrication and cyto-compatibility of Fe_3O_4/SiO_2/graphene-CdTe QDs/CS nanocomposites for drug delivery. Colloids Surf B Biointerfaces. 2014;117:466-472.
109. Padhi, D.K., Panigrahi, T.K., Parida, K., Singh, S.K. and Mishra, P. M., "Green synthesis of Fe_3O_4/RGO nanocomposite with enhanced photocatalytic performance for Cr (VI) reduction, phenol degradation, and antibacterial activity", ACS Sustainable Chemistry & Engineering, Vol. 5, No. 11, (2017), 10551–10562.
110. Peik-See, T., Pandikumar, A., Ngee, L.H., Ming, H.N. and Hua, C. C., "Magnetically separable reduced graphene oxide/iron oxide nanocomposite materials for environmental remediation", Catalysis Science & Technology, Vol. 4, No. 12, (2014), 4396– 4405.
111. Pelin M., Fusco L., León V., Martín C., Criado A., Sosa S., Vázquez E., Tubaro A., and Prato M.: Differential cytotoxic effects of graphene and graphene oxide on skin keratinocytes. Sci. Rep. 7, 1 (2017).
112. Penc B., Hofmann M., Slaski M., Starowicz P and Szytula A: J. Alloy. Compd. 1999, 282, 8-13.
113. Perreault F., De Faria A.F., Nejati S., and Elimelech M.: Antimicrobial properties of graphene oxide nanosheets: Why size matters. ACS Nano 9, 7226 (2015).
114. Pistofidis N, Vourlias G, Konidaris S, Pavlidou E, Stergiou A, Stergioudis G. The effect of bismuth on the structure of zinc hot-dip galvanized coatings. Materials Letters. 2007; 61(4):994-997. DOI: 10.1016/j.matlet.2006.06.029.
115. Qiao, R; Yang, C.; Gao, M. J. Mater, Chem. 2009, 19, 6274.
116. Qin S., Xiao W., Zhou C., Pu Q., Deng X., Lan L., Liang H., Song X., Wu M., Signal Trans. Target Ther. 2022, 7, 199.
117. Ramanathan, S.; SasiKumar, M.; Radhika, N.; Obadiah, A.; Durairaj, A.; Helen Swetha, G.; Santhoshkumar, P.; Sharmila Lydia, I.; Vasanthkumar, S., Musa paradisiaca reduced graphene oxide (BRGO) /MWCNT-Fe_3O_4 nanocomposite for supercapacitor and photocatalytic applications. Materials Today: Proceedings 2021, 47, 843-85. https://doi.org/10.1016/j.matpr.2021.01.706.
118. Rezapour, M., 2018. One-step electrochemical synthesis and characterization of high performance magnetite/reduced graphene oxide nanocomposite. Anal. Bioanal. Electrochem. 10, 450-464.

rGO-Fe_3O_4 hybrid nanocomposite for removal of Pb (II) via magnetic separation", Chemical Research in Chinese Universities, Vol. 31, No. 4, (2015), 508–513.

119. Riana, M., Sembiring, T., Situmorang, M. Kurniawan, C., Setiadi, E. A., Tetuko, A. P., et al. (2018). Preparation and Characterization of Natural Iron Sand from Kata Beach, Sumatera Barat Indonesia with High Energy Milling (HEM). Jurnal Natural, 97-100.
120. Ribeiro M., Monteiro F. J., Ferraz M. P., Biomatter 2012, 2, 176.
121. Santos C.M., Mangadlao J., Ahmed F., Leon A., Advincula R.C., and Rodrigues D.F.: Graphene nanocomposite for biomedical applications: Fabrication, antimicrobial and cytotoxic investigations. Nanotechnology 23, 395101 (2012).
122. Saurabh Singh, Rakesh K. Sahoo, Nanasaheb M. Shinde, Je Moon Yun, Rajaram S. Mane, Wonsub Chung and Kwang Ho Kim. Asymmetric faradaic assembly of Bi_2O_3 and MnO_2 for a high-performance hybrid electrochemical energy storage device. Received 14th August 2019 Accepted 20th September 2019 DOI: 10.1039/c9ra06331e rsc.
123. Setiadi, E. A., Yunus, M., Nababan, N., Simbolon, S., Kurniawan, C., Humaidi, S., et al. (2017). The Effect of Temperature on Synthesis of $MgFe_2O_4$ Based on Natural Iron Sand by Co-precipitation Method as Adsorbent Pb Ion. Journal of Physics: Conference Series, Vol. 985, pp.012046.
124. Sharma, N., Sharma, V., Jain, Y., Kumari, M., Gupta, R., Sharma, S. K., Sachdev, K., 2017. Synthesis and Characterization of Graphene Oxide (GO) and Reduced Graphene Oxide (rGO) for Gas Sensing Application. Macromol. Symp. 376(1), 1700006. http://doi.org/10.1002/masy.201700006.
125. Sharma, N; Sharma, V; Sharma, S.K; Sachdev, K. Synthesis and Characterization of Graphene Oxide (GO) and Reduced Graphene Oxide (rGO) for Gas Sensing Application. Macromol. Symp. 2017, 376, 1700006. DOI: 10.1002/masy.201700006.
126. Simeonidis K., Mourdikoudis S., Moulla M., et al., J. Magnetism and Magnetic Materials., 316(2), e1(2007), DOI: 10.1016/j.jmmm.2008.01.028.
127. Somvanshi, S.B., Khedkar, M.V., Kharat, P.B., Jadhav, K.M., 2020. Influential diamagnetic magnesium (Mg^{2+}) ion substitution in nano-spinel zinc ferrite ($ZnFe_2O_4$): Thermal, structural, spectral, optical and physisorption analysis. Ceramint. 46(7), 8640-8650. http://doi.org/10.1016/j.ceramint.2019.12.097.
128. Su J., Cao M. H., Ren L., Hu C. W., J. Phys. Chem. C 2011, 115, 14469.
129. Su shiung Lam, Van-Huy Nguyen, Minh Tuan Nguyen Dinh, Dinh Quang Khieu, Duc Duong La, Huu Trung Nguyen, Dai Viet N. Vo, Changlei Xia, Rajender S. Varma, Mohammadreza, Shokouhimehr, Chinh Chien Nguyen, Quyet Van Le and Wanxi Peng, Mainstream avenues for boosting graphitic carbon nitride efficiency: towards enhanced solar light-driven photocatalytic hydrogen production and environmental remediation. Journal of Materials Chemistry A, 2020. 8(21) p. 10571-10603. https://doi.org/10.1039/D0TA02582H.
130. Sun, J., Zhou, S., Hou, P., Yang, Y., Weng, J., Li, X., Li, M., 2006. Synthesis and characterization of biocompatible Fe_3O_4 nanoparticles. J. Biomed. Mater. Res. A, 80(2), 333-41. http://doi.org/10.1002/jbm.a.30909.
131. Sun, X.J., Liu, F.T., Jiang, Q.H., 2011. Synthesis and Characterization of Co^{2+} -Doped Fe_3O_4 Nanoparticles by the Solvothermal Method. Mater. Sci. Forum 688, 364-369. http://doi.org/10.4028/www.scientific.net/msf.688.364.
132. Sun, Y.F., Chen, W.K., Li, W.J., Jiang, T.J., Liu, J.H. and Liu, Z. G., "Selective detection toward Cd^{2+} using Fe_3O_4/RGO nanoparticle modified glassy carbon electrode", Journal of Electroanalytical Chemistry, Vol. 714, (2014), 97–102.
133. Takaobushi, J.; et al. Electronic Structures of $Fe_{(3-x)}M_{(x)}O_{(4)}$ (M=Mn, Zn) Spinel Oxide Thin Films Investigated by X-Ray Photo emission Spectroscopy and X-Ray Magnetic Circular Dichroism. Phys. Rev. B 2007, 76, 205108.
134. Tang N.J., Zhong W., Jiang H.Y., Nanostructured magnetite (Fe_3O_4) thin films prepared by sol-gel method, J. Magn. Magn. Mater.282(2004) 92-95.
135. Tang, L. H., Wang, Y., Li, Y. M., Feng, H. B., Lu, J., Li, J. H., Adv. Funct. Mater. 2009, 19, 2782–2789.

136. Tripathy, D.; Adeyeye, A. O. ; Boothroyd, C. B.; Piramanayagam, S. N. Magnetic and Transport Properties of Co-Doped Fe_3O_4 Films. J. Appl. Phys. 2007, 101, 013904.
137. Tsai M. S.: Mat. Sci. Eng. B, 2004, 110, 132-134.
138. Van-HuyNguyen, Ba-Son Nguyen, Zhong Jin, Mohammadreza, Shokouhimehr, Ho Won Jang, Chechia Hu, Pardeep Singh, Pankaj Raizada, Wanxi Peng, Su Shiung Lam, Changlei Xia, Chinh Chien Nguyen, Soo Young Kim and Quyet Van Le, Towards artificial photosynthesis: Sustainable hydrogen utilization for photocatalytic reduction of CO_2 to high-value renewable fuels. Journal of Chemical Engineering, 2020. 402. p. 126184. https://doi.org/10.1016/j.cej.2020.126184.
139. Vermisoglou, E.C., Jakubec, P., Bakandritsos, A., Pykal, M., Talande, S., Kupka, V., Zboril, R., Otyepka, M. Chemical Tuning of Specific Capacitance in Functionalized Fluorographene. Chem. Matter., 2019, 31(13), 4698-4709.
140. Vijayalakshmi, L. Noor Ul Haq, Mater. Today Commun. 2021, 26, 101835.
141. Wang Z, Luo W, Yan S, Feng J, Zhao Z, Zhu Y, Li Z, Zou Z. $BiVO_4$ nano–leaves: Mild synthesis and improved photocatalytic activity for O2 production under visible light irradiation. CrystEngComm. 2011;13(7):2500-2504. DOI: 10.1039/C0CE00799D.
142. Wang, H., Yuan, X., Wu, Y., Chen, X., Leng, L., Wang, H., Li, H. and Zeng, G., "Facile synthesis of polypyrrole decorated reduced graphene oxide–Fe_3O_4 magnetic composites and its application for the Cr (VI) removal", Chemical Engineering Journal, Vol. 262, (2015), 597–606.
143. Wang, J., Tang, B., Tsuzuki, T., Liu, Q., Hou, X. & Sun, L. 2012. Synthesis, characterization and adsorption properties of superparamagnetic polystyrene/Fe_3O_4/graphene oxide. Chem. Eng. J. 204, 258–263.
144. Wang, W.P., Yang, H., Xian, T., Jiang, J.L., 2012. XPS and Magnetic Properties of $CoFe_2O_4$ Nanoparticles Synthesized by a Polyacrylamide Gel Route. Mater.Trans. 53(9), 1586-1589. http:// doi.org/10.2320/matertrans.m2012151.
145. Wang, X. L., Bai, H., Jia, Y. Y., Zhi, L. J., Qu, L. T., Xu, Y. X., Li, C., Shi, G. Q., RSC Adv. 2012, 2, 2154–2160.
146. Wang, X. L., Bai, H., Yao, Z. Y., Liu, A. R., Shi, G. Q., J. Mater. Chem. 2010, 20, 9032–9036.
147. Wang, Y., Li, Z. H., Hu, D. H., Lin, C. T., Li, J. H., Lin,Y. H., J. Am. Chem. Soc. 2010, 132, 9274-9276.
148. Wang, Y., Shao, Y. Y., Matson, D. W., Li, J. H., Lin, Y. H., ACS Nano 2010, 4, 1790–1798.
149. Wang, Z. H., Xia, J. F., Zhu, L. Y., Chen, X. Y., Zhang, F. F., Yao, S. Y., Li, Y. H., Xia Y. Z., Electroanalysis 2012, 23, 2463–2471.
150. Wang, Z. H., Xia, J. F., Zhu, L. Y., Zhang, F. F., Guo, X. M., Li, Y. H., Xia, Y. Z., Sens. Actuators B: Chem. 2012, 161, 131–136.
151. Wu Z. Y., Xu X. X., Hu B. C., Liang H. W., Lin Y., Chen L. F., Yu S. H., Angew. Chem. 2015, 54, 8179.
152. Wu, K. Q.; Xu, Y.; Yao, Z.; Liu, A.; Shi, G. Supercapacitors based on flexible graphene/polyaniline nanofiber composite films. ACS Nano 2010, 4, 1963–1970.
153. Xu Z. C., Shen C.M., Hou Y.L., Gao H.J., Sun S.H., Oleylamine as both reducing agent and stabilizer in a facile synthesis of magnetite nanoparticles, Chem. Mater.21 (2009) 1778-1780.
154. Xu, J.-J.; Chen, M.-D.; Fu, D.-G. Preparation of bismuth oxide/titania composite particles and their photocatalytic activity to degradation of 4-chlorophenol. Trans. Nonferrous Met. Soc. China 2011, 21, 340–345.
155. Yadav, R. S., Kuritka, I., Vilcakova, J., Masilko, J., Kalina, L., et al. (2017). Structural, Magnetic, Dielectric and Electric Properties ov $NiFe_2O_4$ Spinel Ferrite Nanoparticles Prepared by Honey- Mediated Sol-Gel Combustion. Journal of Physical and Chemistry of Solids, 1-42.
156. Yang W., Ratinac K. R., Ringer S. P., Thordarson P., Gooding J. J., Braet F., Angew. Chem. Int. Ed. 2010, 49, 2114.

157. Yang X., Zhang X., Ma Y., Huang Y., Wang Y., Chen Y., Superparamagnetic graphene oxide–Fe_3O_4nanoparticles hybrid for controlled targeted drug carriers, J. Mater. Chem. 19 (18) (2009) 2710–2714, https://doi.org/10.1039/b821416f.
158. Yang Z., Hao X., Chen S., Ma Z., Wang W., Wang C., Yue L., Sun H., Shao Q., Murugadoss V., and Guo Z.: Long-term antibacterial stable reduced graphene oxide nanocomposites loaded with cuprous oxide nanoparticles. J. Colloid Interface Sci. 533, 13 (2019).
159. Yang, H.-M.; Lee, H. J.; Jang, K.-S.; Park, C. W.; Yang, H. W.; Heo, W. D.; Kim, J.-D.J. Mater. Chem. 2009, 19, 4566.
160. Yang, H.-M.; Lee, H. J.; Park, C. W.; Yoon, S. R.; Lim, S.; Jung, B. H.; Kim, J.-D. Chem. Commun. 2011, 47, 5322.
161. Yang, L., Tian, J., Meng, J., Zhao, R., Li, C., Ma, J. and Jin, T., "Modification and characterization of Fe_3O_4 nanoparticles for use in adsorption of alkaloids", Molecules, Vol. 23, No. 3, (2018), 176–185.
162. Yang, S., Zeng, T., Li, Y., Liu, J., Chen, Q., Zhou, J., Ye, Y. and Tang, B., "Preparation of graphene oxide decorated Fe_3O_4@ SiO_2 nanocomposites with superior adsorption capacity and SERS detection for organic dyes", Journal of Nanomaterials, Vol. 16, No. 1, (2015), 1–8.
163. Yao, Y., Miao, S., Liu, S., Ma, L. P., Sun, H. & Wang, S. 2012. Synthesis, characterization, and adsorption properties of magnetic Fe_3O_4:graphene nanocomposite. Chem. Eng. J. 184, 326–332.
164. Yavuz, C.T., Mayo, J.T., Yu, W.W., Prakash, A., Falkner, J.C., Yean, S., Cong, L., Shipley, H.J., Kan, A., Tomson, M., Natelson, D., Colvin, V.L., 2006. Low-Field Magnetic Separation of Monodisperse Fe3O4 Nanocrystals. Sci. 314(5801), 964– 967. http://doi.ord/10.1126/science.1131475.
165. Yu, L., Wu, H., Wu, B., Wang, Z., Cao, H., Fu, C. and Jia, N., "Magnetic Fe_3O_4-reduced graphene oxide nanocompositesbased electrochemical biosensing", Nano-Micro Letters, Vol. 6, No. 3, (2014), 258–267.
166. Zhang H, Xie AJ, Wang CP, Wang HS, Shen YH, Tian XY. Room temperature fabrication of an RGO-Fe_3O_4 composite hydrogel and its excellent wave absorption properties. RSC Advances. 2014;4(28):14441-14446.
167. Zhang Y., Yang Y., Dong Z., Shen J., Song Q., Wang X., Mao W., Pu Y., Li X., J. Mater. Sci. Mater. Electron. 2020, 31, 15007.
168. Zhang Z., Dou M., Liu H., Dai L., Wang F., Small 2016, 12, 4193.
169. Zhang, Y., Tang, Y., Li, S., Yu, S., Chem. Eng. J. 2013, 222, 94–100.
170. Zhao G, Mo Z, Zhang P, et al. Synthesis of graphene/ Fe_3O_4/NiO magnetic nanocomposites and its application in photocatalytic degradation the organic pollutants in wastewater[J]. Journal of Porous Materials, 2015, 22/5: 1245-1253.
171. Zhao, G., Song, S., Wang, C., Wu, Q., Wang, Z., Anal. Chim. Acta 2011, 708, 155–159.
172. Zhou GM, Wang DW, Li F, et al. Graphene-wrapped Fe_3O_4 anode material with improved reversible capacity and cyclic stability for lithium ion batteries. Chem Mater. 2010; 22(18): 5306-5313.
173. Zhou W., Tang K., Zeng S., and Qi Y., Nanotechnology, 19(6), (2008), DOI:10.1088/0957-4484/19/6/065602.